Journal of Geophysical Research: Oceans

RESEARCH ARTICLE
10.1029/2017JC013064

Three-Dimensional Modeling of Fine Sediment Transport by Waves and Currents in a Shallow Estuary

Yi-Ju Chou[1,2,3], Kurt S. Nelson[4], Rusty C. Holleman[5], Oliver B. Fringer[4], Mark T. Stacey[6], Jessica R. Lacy[7], Stephen G. Monismith[4], and Jeffrey R. Koseff[4]

[1]Institute of Applied Mechanics, National Taiwan University, Taipei, Taiwan, [2]Taida Institute of Mathematical Science, National Taiwan University, Taipei, Taiwan, [3]Ocean Technology Research Center, National Taiwan University, Taipei, Taiwan, [4]Bob and Norma Street Environmental Fluid Mechanics Laboratory, Department of Civil and Environmental Engineering, Stanford University, Stanford, CA, USA, [5]San Francisco Estuary Institute, Richmond, CA, USA, [6]Department of Civil and Environmental Engineering, University of California Berkeley, Berkeley, CA, USA, [7]Pacific Coastal and Marine Science Center, U.S. Geological Survey, Santa Cruz, CA, USA

Key Points:
- 3-D wave-coupled modeling of suspended sediment transport in South San Francisco Bay is conducted
- The model shows a stark contrast between the behavior of the SSC on the shoal and in the deep channel
- The two-size floc model is shown to be capable of predicting suspended sediment concentration in the Bay

Correspondence to:
Y.-J. Chou,
yjchou@iam.ntu.edu.tw

Citation:
Chou, Y.-J., Nelson, K. S., Holleman, R. C., Fringer, O. B., Stacey, M. T., Lacy, J. R., et al. (2018). Three-dimensional modeling of fine sediment transport by waves and currents in a shallow estuary. *Journal of Geophysical Research: Oceans*, *123*. https://doi.org/10.1029/2017JC013064

Received 5 MAY 2017
Accepted 28 APR 2018
Accepted article online 6 MAY 2018

Abstract A suspended sediment transport model is implemented in the unstructured-grid SUNTANS model and applied to study fine-grained sediment transport in South San Francisco Bay. The model enables calculation of suspension of bottom sediment based on combined forcing of tidal currents and wind waves. We show that accurate results can be obtained by employing two-size classes which are representative of microflocs and macroflocs in the Bay. A key finding of the paper is that the critical calibration parameter is the ratio of the erosion of the microflocs to macroflocs from the bed. Different values of this erosion ratio are needed on the shallow shoals and deeper channels because of the different nature of the sediment dynamics in these regions. Application of a spatially variable erosion ratio and critical shear stress for erosion is shown to accurately reproduce observed suspended sediment concentration at four-field sites located along a cross-channel transect. The results reveal a stark contrast between the behavior of the suspended sediment concentration on the shoals and in the deep channel. Waves are shown to resuspend sediments on the shoals, although tidal and wind-generated currents are needed to mix the thin wave-driven suspensions into the water column. The contribution to the suspended sediment concentration in the channel by transport from the shoals is similar in magnitude to that due to local resuspension. However, the local contribution is in phase with strong bottom currents which resuspend the sediments, while the contribution from the shoals peaks during low-water slack tide.

1. Introduction

Understanding sediment transport is important in estuarine and coastal environments from a number of perspectives because sediment budgets regulate hydrological processes, morphology, and ecological function over a wide range of spatial and temporal scales. Transport and fate of heavy metals and other contaminants depends to great extent on the fate of sediments, particularly fine-grained sediments in estuaries. Suspended sediment transport also regulates ecological function, since nutrients bind to fine sediments, and high turbidity limits sunlight penetration in the water column, thereby controlling phytoplankton production (Cloern, 1987). Sedimentation in shallow waters forms wetlands and intertidal mudflats that support critical habitats for a wide range of plant and animal species. Wetlands also offer an important buffer that protects inland infrastructure against threats induced by storm surge. Therefore, understanding sediment transport and the associated morphological change through accurate modeling is essential for informed management planning related to coasts and estuaries.

Successful modeling of estuarine sediment dynamics hinges on the accuracy of two primary modeling components. First, a validated hydrodynamics model that captures hydrodynamic forcing over a wide range of temporal scales is essential. These time scales range from tidal time scales to surface wave and turbulence time scales. Because the spatial and temporal resolutions employed by a field-scale model do not allow for the resolution of waves and turbulence, capturing those effects requires a wave model, such as the wave-action approach of SWAN (Simulating WAves Nearshore; Booij et al., 1999), and a turbulence model via the Reynolds-Averaged Navier-Stokes (RANS) formulation. The most common RANS models are the two-equation

approaches, including $k-kl$ (Mellor & Yamada, 1982), $k-\epsilon$ (Rodi, 1984), $k-\omega$ (Wilcox, 1988), and the generic length scale formulation of Umlauf and Burchard (2003), which were compared by Warner et al. (2005). In addition to the effects of turbulence and waves, simulations over longer time scales may be impacted by the effects of climate change (Bonaldo et al., 2015). Models of complex sediment dynamics including erosion, suspension, deposition, the resulting morphological changes, hydrodynamic feedbacks, and so on, are necessary. While hydrodynamics models have progressed remarkably in recent years due to advances in numerical and computational techniques, including structured-grid models such as POM (Blumberg & Mellor, 1987), ROMS (Shchepetkin & McWilliams, 2005), and Delft3D (Deltares, 2018a), and unstructured-grid models such as DFLOW-FM (Deltares, 2018b), FVCOM (Chen et al., 2003), SUNTANS (Fringer et al., 2006), and SCHISM (Zhang et al., 2016), accurate modeling of sediment dynamics remains elusive. Unlike hydrodynamics that can be mathematically described with the Navier-Stokes equations along with continuity, the behavior of a sediment-water mixture in either (concentrated) near-bed regions or (dilute) water columns is still poorly understood. A primary cause of the complex behavior of sediment mixtures in estuaries is the small particle size. In shallow estuaries, bed sediments consist primarily of silt and clay which are comprised of particles with grain sizes ranging from O(1–63 μm). An important characteristic of fine-grained sediments is the influence of interparticle forces that result in flocculation and hindered settling of suspensions (Winterwerp & van Kesteren, 2004) and consolidation of the bed, processes that are extremely difficult to model accurately. As a result, due to a lack of theories for the behavior of cohesive sediments, existing sediment transport models rely on empirical or semiempirical parameterizations of the observed phenomena (e.g., Son & Hsu, 2011; Winterwerp, 1998), and model accuracy varies significantly depending on the particular hydrodynamic conditions and sediment properties. Therefore, cohesive and noncohesive (coarse) sediment transport is modeled with varying degrees of complexity and accuracy.

Recently, owing to great advances in computational power, three-dimensional models are commonly employed, yet the differences between different three-dimensional implementations depends to great extent on the range of physical processes that are incorporated. Gessler et al. (1999) presented a 3-D sediment transport model, CH3D-SED, and applied it to the lower Mississippi River. They considered sediment suspended exclusively by tidal currents. However, it has been well documented that wind-generated surface waves can be a major forcing mechanism driving sediment entrainment. Lee et al. (2004) incorporated wave effects by adding the wave-induced shear stress as a function of the input wind speed, wind direction, and water depth. In wave-dominated estuarine environments, wave-current interaction also plays an important role in the hydrodynamics. In order to capture wind-wave effects more accurately, hydrodynamics models typically incorporate spectral wave models that calculate mean wave properties by simulating transport of wave-action density in spectral and geographical spaces. For example, Carniello et al. (2005) incorporated a finite-element shallow-water model with a monochromatic wave model to study hydrodynamics in Venice lagoon, Italy. Since the development of the SWAN wave model (Booij et al., 1999), extensive effort has been made to couple SWAN with various ocean circulation models to study wave-current interactions (Haas & Warner, 2009; Huang et al., 2010; Sheng & Liu, 2011). Recently, with the addition of atmospherical coupling for storm-surge modeling, Warner et al. (2010) developed the COAWST (coupled ocean-atmosphere wave sediment transport) modeling system, which couples three distinct models for the atmosphere, currents, and waves in a two-way fashion. Examples of the COAWST application are given in Carniel et al. (2016), and presented in references therein.

This paper presents a modeling strategy for fine sediment transport in estuaries. The focus is on South San Francisco Bay (herein referred to as South Bay), which is a typical shoal-channel estuarine system, with shoals of depth 2–4 m and a narrow channel of depth 13–15 m. In general, the shallow regions of the estuary allow for the interaction between the wind-induced surface gravity waves and the muddy bottom, resulting in a great amount of sediment resuspension from the bottom into the water column. The deep water channel acts as a conduit, which transports suspended sediment by the energetic flow. Hence, mass exchange between the channel and shoals is a key factor in understanding the sediment budget in a shoal-channel estuary. Considerable research has focused on sediment transport in North San Francisco Bay (e.g., Bever & MacWilliams, 2013; Ganju et al., 2009; Higgins et al., 2007; McKee et al., 2006; van der Wegen et al., 2011b), but modeling studies on South Bay are relatively rare. The earlier South Bay studies by Lacy et al. (1996) and Schoellhamer (1996) show strong correlation between high SSC and strong-wind events, suggesting a pronounced contribution of wind-driven currents. In South Bay, persistent westerly to northwesterly

winds during the summer and fall months can cause surface flows to the southeast, resulting in wind setup, which then produces return flows to the northwest in the deep water channel (Walters et al., 1985). The resulting sediment fluxes are directed toward the southeast in the shallows and northwest in the deep channel. Lacy et al. (1996) also suggested wind waves as a mechanism for resuspension of bottom mud during the low-water period preceding the flood tide, making SSC higher on average during flood tides. A more recent study by Brand et al. (2010) found that most resuspension events occurred during flood tides that followed wave events during low water, which confirmed the key role of wind waves in resuspension of the bottom mud. Based on a comparison between the measured SSC at different sites, Brand et al. (2010) also show strong spatial variability of SSC in South Bay. To model the SSC at a shallow shoal in South Bay, a one-dimensional vertical (1−DV) model was proposed by Brand et al. (2015) which models vertical turbulent mixing and settling of two sediment size classes. After calibrating the settling velocity of a "fast-settling" size class and a "slowly settling" size class, the approach gives good predictions of SSC. Using the same data set, Lacy et al. (2014) demonstrated that baroclinic forcing due to lateral sediment-driven density gradients could drive lateral sediment fluxes during two strong-wind events in Fall of 2009. Sediment-induced stratification also has the potential to damp turbulence, as demonstrated by MacVean and Lacy (2014) in North San Francisco Bay, where turbulence damping was observed in the presence of vertical stratification due to strong wind-wave resuspensions.

These previous studies reveal key factors influencing the sediment budget in South Bay, including tidal advection, wind-induced surface currents, gravity waves, and density-driven flows, all of which lead to strong spatial and temporal variability in the estuary. Because they were all conducted with point measurements, they highlight the need for a three-dimensional modeling system that gives a better understanding of the transport mechanisms in South Bay. To this end, the present paper focuses on addition of a fine-grained sediment transport model to the unstructured-grid, finite-volume SUNTANS model. Following the previous modeling study by Ganju et al. (2009) and Brand et al. (2015), as well as the field measurement by Manning and Schoellhamer (2013), a two-size sediment transport model that divides cohesive sediments into microflocs and macroflocs is employed. In addition, a bed-layer model that allows for nonuniform erodibility for suspended sediment is also presented. Previously, the hydrodynamics model has been incorporated with a spectral wave model, and waves are forced with a spatially interpolated wind field from five wind stations (Chou et al., 2015). The calibrated modeling system in the present study reveals interesting features of the spatial distribution of SSC due to wave and tidal forcing. Furthermore, by tuning the bed erodibility, model results demonstrate important mechanisms related to shoal-channel exchange. We describe the development of a multiclass advection-diffusion model to calculate transport of suspended sediment along with a multilayer bed model that includes the effects of both erosion and consolidation. The resulting modeling system is able to predict sediment transport driven by both tides and waves, which we show through application of the model to understand the dynamics of suspended sediments in South Bay. The suspended sediment and bed models are outlined in section 2, while the model setup and sensitivity to the sediment parameters are presented in section 3. Results are presented in section 4, along with discussion of tidal and wave-induced suspension as well as the shoal-channel exchange. Summary and conclusions are presented in section 5.

2. Model Description

2.1. Suspended Sediment Concentration

The standard approach to model transport of dilute suspended sediment is to employ the advection-diffusion equation along with a constant settling velocity w_s, which represents the terminal fall velocity of a single sediment grain in a quiescent fluid. The settling velocity is a function of both sediment and fluid properties and, when concentration is sufficiently high, a function of sediment concentration. For a single spherical particle, the settling velocity w_{s0} can be approximated from Stokes' law. For cohesive sediment, particles can aggregate due to interparticle forces or chemical bonds to form a new unit, which is called a floc. This makes it a difficult task to model settling of cohesive sediment. For example, in the mud transport module of the coastal model MIKE21 (DHI, 2007), once sediment concentration exceeds the critical value for which flocs can form, the settling velocity exponentially increases with concentration. However, according to recent measurement in San Francisco Bay (Manning & Schoellhamer, 2013), no significant correlation between settling velocity and concentration was found. Therefore, in the present model, we use a multiclass

suspended sediment transport model to calculate transport of suspended sediments of different sizes. The transport equation for the concentration of sediment size class q, C_q (in mg L^{-1}) is given by

$$\frac{\partial C_q}{\partial t}+\nabla\cdot(\mathbf{u}C_q)-\frac{\partial}{\partial z}(w_{s,q}C_q)=\nabla_H\cdot(\gamma_H\nabla_H C_q)+\frac{\partial}{\partial z}\left(\gamma_V\frac{\partial C_q}{\partial z}\right), \tag{1}$$

where $\mathbf{u}$ is the three-dimensional velocity vector, ∇_H is the horizontal gradient operator, and γ_H and γ_V are the horizontal and vertical eddy-diffusivities. We ignore γ_H because its effects are negligible when compared to horizontal dispersion induced by advection that is resolved by the model. The vertical eddy-diffusivity is obtained with $\gamma_V=\nu_T/\sigma_T$, where ν_T is the eddy-viscosity obtained from the turbulence model and σ_T is the turbulent Schmidt number and is typically $O(1)$ (Nielsen & Teakle, 2004; van Rijn, 1984). Following the successful modeling work for San Francisco Bay by Chua and Fringer (2011), the Mellor-Yamada level 2.5 (MY2.5) (Mellor & Yamada, 1982) turbulence closure scheme with stability functions and the wall function of Blumberg et al. (1992) is used to compute ν_T in the present study. This closure scheme has been shown to predict the same SSC profiles in steady open channel flows as predicted by theory and other closure schemes (Warner et al., 2008), including the $k-\epsilon$ model. Although it is possible to parameterize the Schmidt number based on sediment and flow properties (Dyer & Soulsby, 1988), we ignore this second-order effect and assume $\sigma_T=1$. After calculating concentration of each size class using equation (1), the total suspended sediment concentration (SSC) is obtained with

$$SSC=C_{total}=\sum_{q=1}^{N_s}C_q, \tag{2}$$

where N_s is the number of the size classes. In equation (1), different size classes are associated with different settling velocities, $w_{s,q}$. For noncohesive sediments, these can be obtained from Stokes' law with different particle sizes. However, for cohesive sediments, settling velocities obtained from field observations should be used. If there are no field observations, the settling velocity of a single floc can be estimated using the fractal model of Kranenburg (1994). When the SSC of fine-grained sediments (which consist primarily of flocs) reaches a particular level, settling of flocs is hindered (Scott, 1984). The settling velocity thus becomes a function of volumetric sediment concentration (ϕ_f). To account for this effect, once the local concentration exceeds a critical value C_{hinder} ($\phi_f\approx 0.01$ in volume fraction) (Winterwerp & van Kesteren, 2004) for which hindered settling occurs, we adopt the popular formula of Richardson and Zaki (1954) to obtain the modified value. Hence, the settling velocity of each size class is given by

$$w_{s,q}=\begin{cases} w_{s0,q}(1-\phi_f)^4 & \text{if } C>C_{hinder} \\ w_{s0,q} & \text{otherwise}\end{cases}. \tag{3}$$

In the present study, $C_{hinder}=26.5$ g L^{-1}.

Because the SSC in South Bay is dominated by flocculated sediments (e.g., Jaffe et al., 2007; Manning & Schoellhamer, 2013), we do not explicitly consider noncohesive sediments (see section 3.2). Instead, based on observations by Manning and Schoellhamer (2013), we employ a two-size sediment transport model to represent microfloc and macrofloc, details of which are given in section 3.2.

2.2. Bed-Sediment Calculation

2.2.1. Sediment Erosion

At the bottom boundary, a sediment flux needs to be specified to model entrainment of sediment from the bed. Ignoring diffusion and horizontal advection for convenience, the finite-volume form of equation (1) in two dimensions (x and z) at the bottom-most cell with length Δx and height Δz can be written as:

$$\frac{dC_q}{dt}+\frac{1}{\Delta z}(w-w_{s,q}C_q)|_{\text{top}}=\frac{1}{\Delta z}(E_{b,q}-w_{s,q}C_q)|_{\text{btm}}, \tag{4}$$

where $E_{b,q}$ is the erosion rate of sediments with size class q from the bed, and subscripts top and btm imply values at the top and bottom faces of the bottom-most cell, respectively. There have been many studies on the empirical formula to describe the erosion rate base on the excess shear stress

$$\Delta\tau_b = \tau_b - \tau_{cr,E}\,, \tag{5}$$

where τ_b is the shear stress exerted by the flow on the bed and $\tau_{cr,E}$ is the critical shear stress for erosion. A comprehensive review of parameterizations for the erosion rate E_b can be found in Sanford and Maa (2001). In the present study, we choose the exponential relation (Parchure & Mehta, 1985)

$$E_b = E_0 \exp\left[\alpha \Delta\tau_b^{\beta}\right], \tag{6}$$

where E_0 is the erodibility and α and β are empirically determined constant coefficients.

The bed shear stress τ_b due to the combined effect of both current and wave forcing is given by (e.g., Grant & Madsen, 1986)

$$\tau_b = \sqrt{\tau_c^2 + \tau_w^2 + 2\tau_c\tau_w \cos\theta_{cw}}\,, \tag{7}$$

where the current-induced (τ_c) and wave-induced (τ_w) bottom stresses are given by

$$\tau_c = \rho C_{D,s} U_{c,0}^2\,, \tag{8}$$

$$\tau_w = \frac{1}{2}\rho f_w U_{orb}^2\,, \tag{9}$$

where θ_{cw} is the angle between currents and waves, $C_{D,s}$ is the drag coefficient induced by the sediments, f_w is the wave friction factor, U_{orb} is the wave-orbital velocity obtained from the wave model, and $U_{c,0} = \sqrt{u_0^2 + v_0^2}$ is the magnitude of the horizontal velocity at the bottom-most cell. The wave-current angle θ_w, wave friction factor f_w, and bottom orbital velocity U_{orb} are obtained from the wave model, as outlined in Chou et al. (2015). Based on the log law, the drag coefficient for the currents in the absence of waves for use in the quadratic drag law (8) is given by

$$C_{D,s} = \left[\frac{1}{\kappa}\ln\left(\frac{z_{btm} + z_0}{z_0}\right)\right]^{-2}, \tag{10}$$

where $\kappa = 0.41$ is the von Karman constant, z_{btm} is the z coordinate of the bottom-most cell, and z_0 is the grain roughness obtained with $z_0 = k_s/30$ and $k_s = 2.5D_0$ is the equivalent Nikuradse bottom roughness. We assume a representative grain size of $D_0 = 100$ μm based on the field observation by Manning and Schoellhamer (2013), who showed that the size of most of the suspended flocs in South Bay ranges from 50 to 300 μm. It is important to note that the drag coefficient $C_{D,s}$ and bed roughness are not the same as those used in the hydrodynamics implementation of Chua and Fringer (2011), which are typically much larger and parameterize the effect of larger-scale unresolved roughness features on the flow.

2.2.2. Multilayer Bed Model

Sediment erosion is controlled by the properties of the bed which also determine the bed resistance to the bottom shear stress exerted by the flow. In our model, this is modeled with the erodibility and a critical shear stress for erosion (see equation (6)). If the bed is composed of freshly deposited flocs, a soft mud or "fluff" layer forms and the associated critical stress is very small (Lick, 2009). This top fluff layer is easily eroded, exposing the more consolidated mud layer below. The sediments in this exposed layer have a higher resistance to the bottom shear stress and are thus more difficult to erode. In order to model this erosion-consolidation processes, a multilayer bed model, like many others, is employed in which the bed is vertically discretized into several layers. Unlike the noncohesive sediment bed model (e.g., Warner et al., 2008), which tracks size fractions of the bed sediments, the present bed model characterizes depth-varying critical shear stress for the soft cohesive sediment deposits (Parchure & Mehta, 1985). The depth-varying critical shear stress at the bed is due to self-weight consolidation of the fine deposits, the behavior of which can be mathematically described using the Gibson equation in a more sophisticated manner (see e.g., Zhou et al., 2016). Rather than to compute the evolution of the thickness of each layer, we compute the evolution of the mass in each layer. This eliminates the need for the sediment dry density which is difficult to measure because it can vary over time and can also be highly spatially heterogeneous. Ignoring changes in bed height is valid for simulations over relatively short time scales which incur minimal changes in the bed elevation.

As it considers fractions of different size classes in each layer, bed models of Warner et al. (2008) and Harris et al. (2008) are faithful representations of the sediment bed, although primarily for noncohesive sediments.

When modeling cohesive sediments in shallow estuaries where the aggregated flocs dominate the suspension, as in San Francisco Bay (Jaffe et al., 2007; Manning & Schoellhamer, 2013), there are no models capable of correctly computing the size distribution in suspension based on erosion in the bed. Indeed, in many cases the size distribution in the bed appears to be unrelated to what is in suspension (Brand et al., 2010). Therefore, to avoid the need to rely on a parameterization for the near-bed particle physics and associated flocculation, which would introduce significant uncertainty into a model owing to the need for many parameters that are difficult to calibrate or measure, we employ relatively simple model that only needs the critical stress and relative fraction of erosion of two-size classes in each layer. This relative fraction is used as a tuning parameter to account for unresolved near-bed flocculation physics. Using this approach, we show that the model gives good agreement with the observations over a spring-neap tidal cycle.

The time evolution of the mass per unit area (M_b) within each layer is calculated with

$$M_{b,j}^{(n+1)} = \begin{cases} \mathrm{Max}\left[0, M_{b,j}^{(n)} + \sum_{q=1}^{N_s} w_{s,q} C_q^{(n)}|_{\mathrm{btm}} \Delta t - \left(E_{b,j}^{(n)} - T_{C,j}^{(n)}\right)\Delta t\right], & j=1=\mathrm{top} \\ \mathrm{Max}\left[0, M_{b,j}^{(n)} - \left(E_{b,j}^{(n)} - T_{C,j}^{(n)}\right)\Delta t\right], & j \neq 1=\mathrm{top} \\ \mathrm{Max}\left[0, M_{b,j}^{(n)} + T_{C,j-1}\Delta t\right], & j=\mathrm{btm} \\ \mathrm{Max}\left[0, M_{b,j}^{(n)} + \left(T_{C,j-1} - T_{C,j}\right)\Delta t\right], & \mathrm{otherwise}, \end{cases} \tag{11}$$

where the subscript j represents the layer index in order from the top ($j = 1$) to the bottom (j=btm), E_b is the erosion calculated via the critical shear stress assigned to each layer, T_C is the consolidation rate modeled as a flux of mass between layers, and $C_q|_{\mathrm{btm}}$ is the concentration of size class q at the bottom-most cell in the water column. Equation (11) shows that erosion occurs only at the surface of the top layer (j= top), and the new deposition of sediment from the water column forms the first layer (j=1= top). The second row on the RHS of equation (11) describes the case when the first top layer ($j = 1$) is depleted, and the erosion persists without deposition. During the calculation, if a layer is eliminated (i.e., $M_{b,j}^{(n+1)}=0$), then the extra erosion becomes the erosion of the next layer. The mass in each layer is initialized with $M_{b,j}=\rho_{bd,j}h_{L,j}$, where $\rho_{bd,j}$ is the sediment dry density of layer j and $h_{L,j}$ is the initial layer depth of layer j. As we investigate hydrodynamics and SSC during a spring-neap tidal cycle, the time scale of which is relatively short compared to that of associated with morphodynamic changes (Roelvink, 2006), conversion back to $h_{L,j}$ to compute the effect of the bed elevation changes is not necessary in the present study while assuming that elevation changes are negligible.

It is difficult to parameterize the individual erosion rates for each size class because there are no parameterizations that can explicitly account for the complex near-bed physics relating the grain size distribution in the bed to what is eroded and subsequently suspended in the water column. In South Bay, for example, the particle-size distribution measured in the water column consists of larger particle sizes than the distributions based on bed samples, suggesting flocculation upon resuspension (Brand et al., 2010). Rather than attempting to parameterize the suspension of each size class, we assume a single erosion rate that represents erosion of all sediment size classes at the bottom boundary, and each bed layer is assigned a different value (see Table 1). For size class q in layer j, using $f_{q,j}$ to indicate the mass fraction, the erosion rate of sediment is given by

$$E_{b,q,j}=f_{q,j}E_{b,j}\,, \tag{12}$$

where $E_{b,j}$ is the total erosion rate, and $\sum_q f_{q,j}=1$. Although relatively crude, this modeling approach provides good comparison of model results to field observations in this study. Furthermore, we set the same $f_{q,j}$ throughout the simulation for each bed layer, which is based on the observation that the floc size distribution in the water column strongly depends on flow conditions (Manning & Schoellhamer, 2013) due to flocculation and breakup processes, rather than the grain size distribution in the bed. The same idea was adopted by Brand et al. (2015), who modeled SSC at a single point in South Bay using a one-dimensional vertical (1-DV) with two sediment size classes. In their model, the settling velocities, fraction of each class, and total erosion rate are obtained from the flux and concentration measurement above the sediment bed.

Table 1
Parameters for the Multilayer Bed Model

Layer no.	ρ_{bd} (g m^{-3})	$\tau_{cr,E}$ (N m^{-2})	α	E_0 (g m^{-2} s^{-1})	β	T_c (g m^{-2} s^{-1})	h_L (m)
1	75,000	0.1	4.5	0.01	1	0.0002	0.1
2	530,000	0.4	4.5	0.01	1	0.0002	0.5
3	1,200,000	1.2	4.5	0.01	1	0.0002	4.0

3. Modeling Sediment Transport in San Francisco Bay

3.1. Model Setup: Hydrodynamics and Waves

The domain setup of Chua and Fringer (2011), who model tidally driven salinity in San Francisco Bay during January of 2005 using SUNTANS, is employed in the present study. Their study showed good agreement compared to observations of surface elevation, depth-averaged velocity, and salinity. Here some important features are described, although more detail can be found in Chua and Fringer (2011). The computational domain spans between the Pacific Ocean and the Sacramentao-San Joaquin River Delta, as shown in Figure 1. There are two open boundaries. One is the ocean boundary at the Pacific Ocean, which extends approximately 40 km from Golden Gate. The other boundary is at the Sacramento-San Joaquin Delta. The complex and interconnected network of tributaries in the delta is represented by a "false delta," which consists of two rectangles (Gross et al., 2005), as shown in Figure 2. This allows specification of inflow conditions from the Delta. We use bathymetric data obtained from the National Geophysical Data Center (NGDC) database. As shown in Figure 3, San Francisco Bay is deepest at the Golden Gate, which is about 110 m. There is a distinct channel that extends throughout the bay along its thalweg, and this channel incises shallow shoals. The channel depth varies from 10 to 30 m while the shoals are usually less than 5 m deep. Although the present study focuses on the South Bay, the simulation domain for the whole Bay following Chua and Fringer (2011) allows us to obtain correct dynamics at the entrance of the South Bay.

The unstructured grid was generated using SMS (Environmental Modeling System, Inc.). The horizontal grid configuration is shown in Figure 2. The average grid resolution based on triangular cell lengths is 50 m. In the vertical, the grid has structured z levels, with a maximum of 60 layers in the deepest portion of the

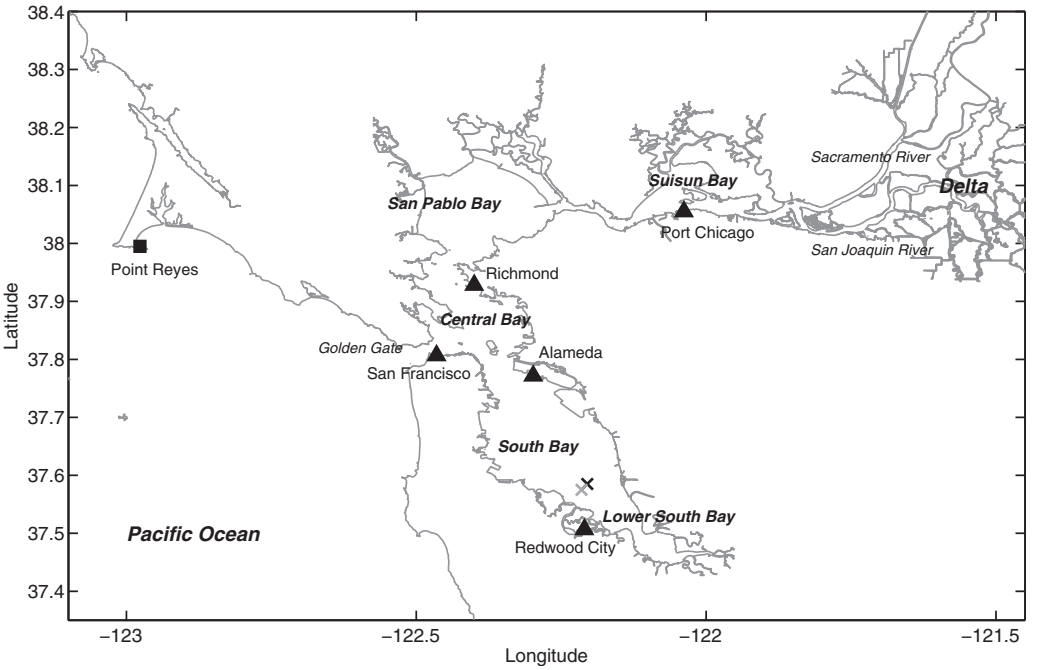

Figure 1. San Francisco Bay coastline along with the locations of wind stations (black triangles), tide gauge (black square), SSC observations on the shoals (black crosses), and SSC observations within the main channel (gray crosses).

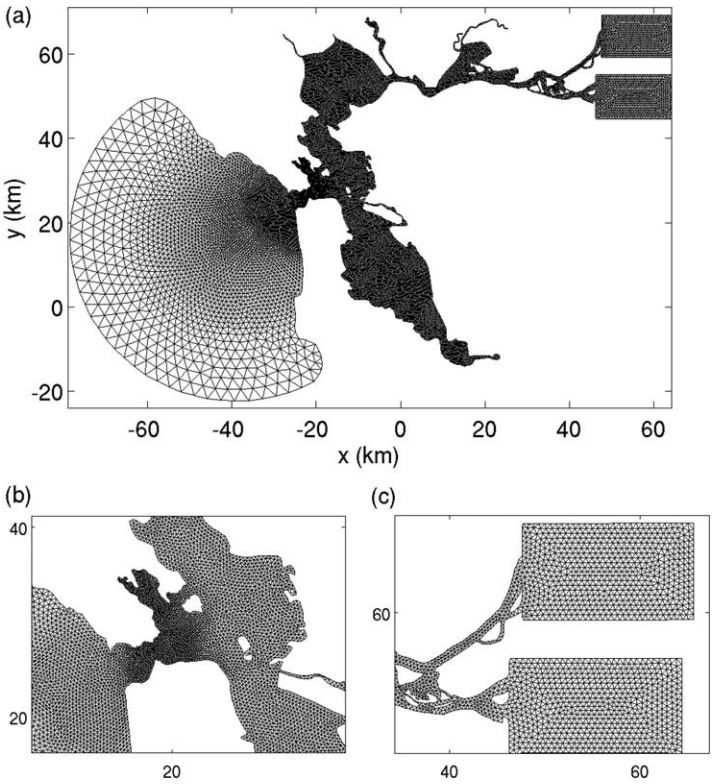

Figure 2. Unstructured grid of San Francisco Bay showing (a) the entire domain, (b) the Golden Gate region, and (c) the rectangular "false delta," following Chua and Fringer (2011). Distances are relative to the channel location in Figure 3.

domain. With a grid stretching ratio of 10% in the z direction, the vertical resolution is refined near the surface, where the minimum vertical grid spacing is 0.29 m. The total number of cells in the horizontal is approximately 80,000 with more than 80% located in the Bay. The three-dimensional grid has approximately 2.5 million grid cells.

The flow is tidally forced by specifying the free-surface elevation along the Pacific Ocean boundary. The surface elevation data at Point Reyes is obtained from the NOAA Center of Operational Oceanographic Products and Services. The flow rate at the Sacramento and San Joaquin Rivers is given by freshwater inflow estimates from the DAYFLOW program (California Department of Water Resources (CDWR), 1986). A time step of 10 s is employed and is dictated by stable horizontal advection of scalars (Fringer et al., 2006) in the hydrodynamics model. Waves are modeled by the wave-action approach as in Booij et al. (1999) on the same grid with the same time step as the hydrodynamics model with wave frequencies ranging from 0.04 to 2 s^{-1} and with wave propagation angles (θ) ranging from 0 to 360°. Both frequency and angle space are discretized with 36 elements and the frequency is distributed logarithmically. Waves and currents are two-way coupled in that wave action is transported by the currents and wave group velocities, while the currents are impacted by the waves through the radiation stresses. Wind speed and direction are reconstructed at each grid cell by interpolating wind data from five NOAA wind stations, as shown in Figure 1. As waves and hydrodynamics are not coupled with a meteorological model, the present coupling method ignores the feedback to the atmosphere and the heat flux at the sea surface. This is valid in the present simulation during which the mild wind events do not result in significant changes in the sea temperature according to the field measurement (Lacy et al., 2014). If the sea temperature changes significantly due to strong-wind events, the heat flux at the ocean-atmosphere boundary cannot be neglected, and the method that couples meteorological, wave, and hydrodynamic models needs to be considered (e.g., Carniel et al., 2016). The historical data in the present study is obtained from the NOAA National Data Buoy Center at a time resolution of 6 min. Therefore, at each simulation time step, wind data are obtained by linear interpolation from two consecutive points in the measured wind time series. More detail on the implementation of the wave model and associated results can be found in Chou et al. (2015).

After a 20 day salinity spin-up period, the model is run for an additional 18 day period beginning on 9 September 2009 and ending on 26 September 2009 (Yeardays 252–269), upon which the waves and sediment transport models are employed. Simulation of the 18 day period requires 155,520 time steps which consumes about 48 h of wallclock time using 24 processors on the Dell PowerEdge M620 supercomputer cluster located at Taida Institute of Mathematical Sciences in Taipei, Taiwan.

3.2. Model Setup: Sediment Transport

3.2.1. Suspended Sediment

In general, there are three dominant size fractions in San Francisco Bay, namely clay, silt, and sand, and these size fractions are highly variable throughout the bay and depend on the local hydrodynamics. Clays and silts are typically categorized as fine sediments that can be suspended while sands and pebbles are coarse-grained sediments that are transported primarily as bed load. Since we focus on SSC, we only consider fine sediments and assume two-size classes based on field measurement by Manning and Schoellhamer (2013), which divide the sediments into microflocs (floc size <160 μm) and macroflocs (floc size ≥ 160 μm). According to Manning and Schoellhamer (2013), the settling velocities of the suspended flocs in South Bay span a wide range from 0.08 to 12 mm s^{-1} with mass-weighted means in six measurements ranging from 0.5 to 6 mm s^{-1}. After testing a few different w_ss within the range of the field data, we use $w_{s,1}=0.1$ mm s^{-1} for the first size class ($q=1$) and $w_{s,2}=2$ mm s^{-1} for the second class ($q=2$). One may

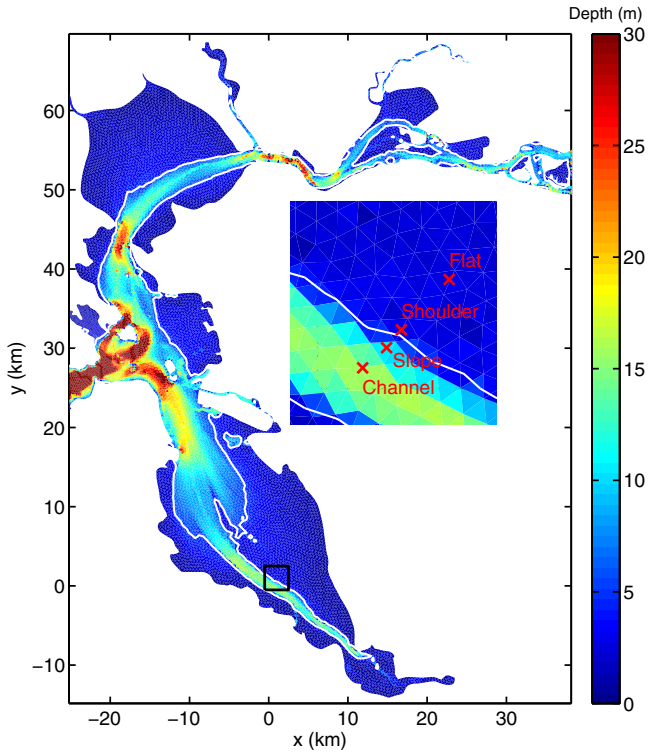

Figure 3. Model bathymetry (in m below MHHW), following Chua and Fringer (2011). The white contours indicate a depth of $d = 5$ m, which is used as the depth to separate shallow-water shoals ($d < 5$ m) from the deep channel ($d > 5$ m). The inset shows a zoomed-in view of the bathymetry within the black rectangle along with the location of the four-field measurement stations.

expect that as w_s increases, the faster settling will result in lower SSC in the model, and vice versa. Although in Manning and Schoellhamer (2013), the settling velocities of suspended flocs in San Francisco Bay are not shown to be a strong function of the floc size, for the sake of simplicity, we refer to the suspended sediment of the first size class as microflocs and the second class as macroflocs. This is consistent with the observation that the small microflocs generally settle at less than 1 mm s^{-1}, while macroflocs settle at 1−15 mm s^{-1} (Mikeš & Manning, 2010). it is possible to model flocculation and breakup in suspension by including source terms on the right-hand side of equation (1) to account for transfer of sediment mass between different floc size classes with the population balance approach (Lick et al., 1992; Sterling et al., 2005). However, such processes are difficult to measure accurately enough to explicitly parameterize their effects in the model and so we do not attempt to include them. Instead, we model cohesive sediment transport via a noncohesive manner (without size exchange) and focus on the importance of the erosion rate of different sediment size classes and show that model skill is highly sensitive to the ratio of erosion of microflocs to macroflocs. The present two-size modeling approach is consistent with Brand et al. (2015), who demonstrated the need for including both "fast-settling" and "slowly settling" SSC components in their 1-DV suspended sediment model.

Because we consider just two-size classes, the relative fraction of each size class in the water column that is eroded from the bed will be given by the ratio of the erosion of the microflocs to macroflocs. This is quantified by the ratio of erosion rates between the two in layer j in the bed and is given by

$$R_{m/M,j} = \frac{f_{1,j}}{f_{2,j}} = \frac{f_{1,j}}{1 - f_{1,j}} \,. \tag{13}$$

This parameter dictates the relative fraction of erosion between the size classes, while E_0, the erodibility, dictates the total erosion of both size classes. Here, we assume constant $f_{q,j}$ (i.e., $R_{m/M}$) in the layers. This can be justified by Manning and Schoellhamer (2013), who found that the size distribution of flocs is more sensitive to flow conditions than it is to the actual distribution within the bed. Moreover, following the results of numerous observations in South Bay (Brand et al., 2010; Collignon & Stacey, 2012, 2013; Lacy et al., 2014) which indicate distinctly different behavior of SSC in deeper channels versus shallow-water shoals, we employ different values of $R_{m/M}$ on the shoals and channels. The shoals are defined as regions of the domain with depths less than 5 m, while the channels are defined as regions of the domain with depths exceeding 5 m (see Figure 3).

3.2.2. Bed Model

We do not initialize the bed layers with an approach that is based on core samples, as is typically done in sediment transport modeling (e.g., Bever & MacWilliams, 2013). In fact, it is difficult to obtain enough samples to produce sufficiently accurate spatial coverage, and sediment cores cannot capture erodibility associated with the fine fluff layer. One option would be to initialize the model with a horizontally uniform bed throughout the domain that has multiple layers, and then allowing the bed model to erode until the critical stress for erosion matches the local time-averaged bed stress throughout the bay. However, the time scales needed to develop such an equilibrium bed are on the order of the residence time within the bay which can be on the order of months or much longer (van der Wegen et al., 2011a; Walters et al., 1985).

Over time, we would expect regions in the bay with higher average bottom stresses to erode down to a depth in which the local critical shear stress for erosion matches the bed stress. As a result, regions subject to high average stresses can have higher resistance to erosion. Given this, rather than running the model over time scales sufficient to ensure bed equilibrium, we initialize the bed-layer thickness based on the spatial distribution of the time-averaged bottom shear stress due to tidal currents, computed with equation (8)

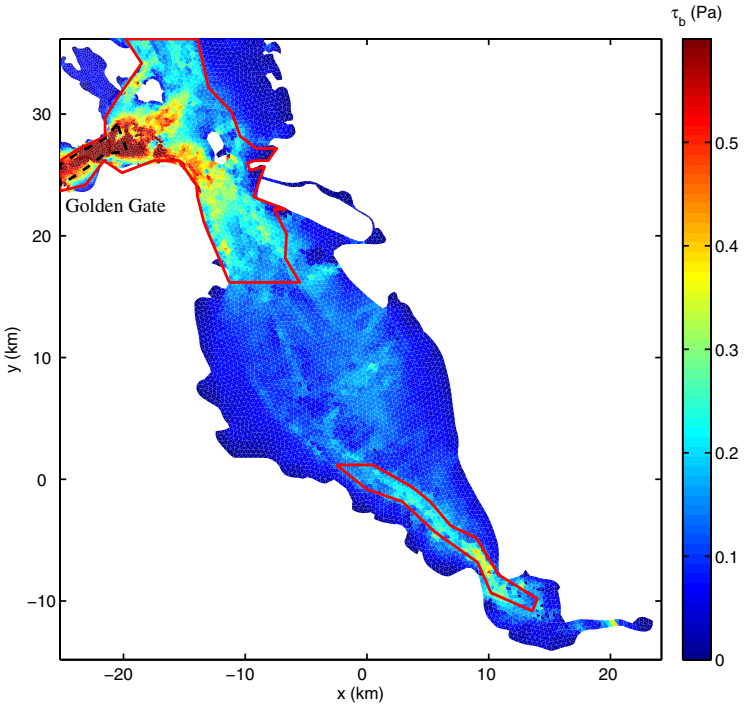

Figure 4. Distribution of the 20 day averaged bottom stress $\langle \tau_b \rangle$ in Central and South Bay along with lines that indicate areas assigned with different critical shear stresses for erosion. The regions enclosed by the red solid lines excluding the region enclosed by the black dashed line correspond to Region II. The region enclosed by the black dashed line near the Golden Gate corresponds to Region III. The regions outside of Regions II or II correspond to Region I.

averaged over the 20 day spin-up period, which we denote as $\langle \tau_b \rangle$. The 20 day period covers a spring-neap cycle, and the obtained $\langle \tau_b \rangle$ represents a mean bottom stress averaged over a sufficiently long-time period. Such a model ignores the impact of waves on the initial bed-layer thickness distribution. However, waves are dominant in the shallows where we expect fine sediments to settle because the settling time is typically shorter than the tidal time scale. In deeper regions where waves are not as important, we expect the tidal currents to dominate erosion, although the water column is deeper and so we do not expect deposition of fine sediments over tidal time scales. Therefore, it suffices simply to initialize the bed-layer thickness distribution based on the time-averaged tidal currents. Because they are strongly depth-dependent, initialization based on tidal currents naturally allows for the fluff layer to exist in the shallows where the fine sediments can settle over tidal time scales, but not in the deeper portions where they do not have time to settle but instead are transported elsewhere. The disparity in settling times and the resulting transport play significant roles in accurately predicting channel and shoal sediment dynamics as discussed in this paper. However, disregarding waves when initializing the bed could underestimate the bed erodibility (i.e., higher $\tau_{cr,E}$ in the model) in the shallows where waves are dominant to excite the bottom mud. A more detailed discussion and demonstration of wave-induced and tide-induced suspension are given in section 4.2. As depicted in Figure 4, we divide the domain into three regions based on the magnitude of $\langle \tau_b \rangle$. The first region (Region I) corresponds to low $\langle \tau_b \rangle$, i.e., $\langle \tau_b \rangle < 0.2$ Pa. This includes all shallow-water shoals and some shallower regions in the channels, such as the upper region (1.175 km $< y <$ 16.175 km) of South Bay. The second region (Region II) is associated with higher $\langle \tau_b \rangle$, i.e., $0.2 < \langle \tau_b \rangle < 0.5$ Pa. This includes some deep water regions in Central Bay

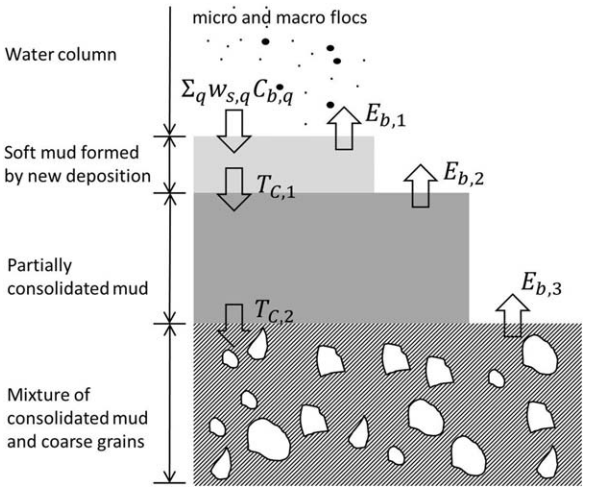

Figure 5. The three-layer bed model which includes the effects of erosion, E, consolidation T_{cr} and settling $w_s C_b$.

Table 2
Summary of Observational Instruments Used to Infer SSC Along With Their Locations

Name	Longitude, E	Latitude, N	Depth (m, MLLW)	Instrument	Height above bottom (m)
Flat	122.20977	37.58632	2.2	ADV	0.35
Shoulder	122.21835	37.57927	2.6	ADV	0.25
Slope	122.21988	37.57673	6.5	ADCP	1.8
Channel	122.22187	37.57397	15.2	ADCP	2.5

and the deep channel in lower South Bay ($y < 1{,}175$ km). The third region (Region III) corresponds to the deepest parts of the Golden Gate channel (depth > 50 m; see Figures 1 and 3), where the largest average bottom stresses ($\langle \tau_b \rangle > 0.5$ Pa) are found.

The three regions defined by the time-averaged bottom stresses dictate the number of layers that are initialized in the bed-layer model. Specifically, areas with low average bottom stresses (Region I) are initialized with all three layers in Table 1. As depicted schematically in Figure 5, the first layer is the soft, easily eroded mud layer that is composed of freshly deposited sediment. The bed is initialized with the bottom two layers in Region II and, to reflect the fact that the top two layers have likely been eroded in Region III, we initialize those regions with just the bottom bed layer in Table 1. The second layer is the partially consolidated mud layer, and the third (bottom) layer is the consolidated layer (see Figure 5). Because sediments are suspended from the top layer, for a relatively short-time simulation during which the initial top layers are retained, a rather simplified model that only considers different $\tau_{cr,E}$ in the Bay but disregards the layered structure would give the same results. However, it neglects properties of cohesive mud on the bed and lacks limitation of erosion, which is essential for long-time simulation. On the other hand, to characterize strong heterogeneity and complexity of sediment transport, the model can be built with more complexities with no limit, but doing this requires more parameters that are highly empirical and unavailable from the field data, which raises model uncertainty. In the present study, based on the framework of the multilayer bed model, we aim to develop a model that is simple but suffices to reproduce the field data to our satisfaction in a spring-neap cycle. This setup of the multilayer bed model is critical for predicting SSC, particularly in the main channel in South Bay. In section 3.4.2, we demonstrate the effects of initializing the domain with a horizontally uniform bed. Parameters for erosion and consolidation of each layer in Table 1 are based on values provided in the MIKE21 model (DHI, 2007) and the case study of Lumborg and Pejrup (2005). Among those parameters except $\tau_{cr,E}$ which determines the threshold of sediment resuspension, adjustment of all the others simply affects the magnitude of the modeled SSC in different manners (see equations (5) and (6)). It should be noted that the present bed model may not be sufficient for simulations over longer time periods when morphological changes are important. In that case, results can be more sensitive to the bed model, and a model that considers different size classes and more layers, such as those of van der Wegen et al. (2011a) and Harris et al. (2008), need to be considered.

Table 3
Micro/Macrofloc Ratios ($R_{m/M}$) Used for Model Calibration Scenarios and Comparison of Skill Scores (SS) in the Channel and Shoal for Each Scenario

		$R_{m/M}$		SS			
Case	Comment	$h < 5$ m	$h \geq 5$ m	Flat	Shoulder	Slope	Channel
S05C43	Base case	0.05	0.43	0.75	0.72	0.66	0.81
S05C43NW	No waves	0.05	0.43	0.46	0.75	0.64	0.76
S00C43	Shoal: Less micro	0.00	0.43	0.40	0.55	0.46	0.51
S11C43	Shoal: More micro	0.11	0.43	0.71	0.56	0.53	0.77
S05C25	Channel: Less micro	0.05	0.25	0.74	0.73	0.64	0.71
S05C67	Channel: More micro	0.05	0.67	0.75	0.70	0.63	0.85
S05C43U	Uniform bed	0.05	0.43	0.79	0.55	0.55	0.25
S05C43NWI	No wind	0.05	0.43				
SNRC43	Shoal: No resuspension	0.00	0.43				
S05CNR	Channel: No resuspension	0.05	0.00				

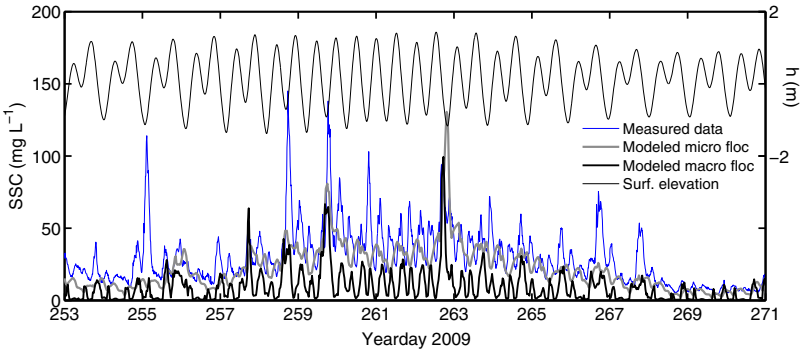

Figure 6. Modeled SSC related to macroflocs and microflocs for the base case (S05C43) compared to observations at the flat station. The modeled surface elevation is also shown for reference.

3.3. Field Data for Model Validation

The model is validated with observations from studies designed to understand wind-enhanced mud suspensions (Brand et al., 2010) and lateral transport at the shoal-channel interface (Collignon & Stacey, 2012, 2013; Lacy et al., 2014) in South Bay. The observations used for validation are located along a lateral transect that covers the shallow-water shoal and deep channel in South Bay (see Figure 1). Two of these are located on the shallow shoals, which we refer to as the "flat" and "shoulder" locations. A third is on the lateral slope of the main channel, referred to as the "slope" location, and the fourth is in the main channel and is referred to as the "channel" location. The water depth at the shoal stations ranges from 2 to 3 m, and in shallow waters resuspension is enhanced by wind waves. In the channel, the mean water depth is roughly 15 m, deep enough so that bottom suspensions are not directly affected by surface waves. Details of the four measurement stations are summarized in Table 2. For more details, including calibration to SSC, see Brand et al. (2010) and Lacy et al. (2014).

The measurements were obtained during the dry seasons of summer and early fall when river inflows are low or absent, and when residence times are on the order of months (Walters et al., 1985). In the absence of appreciable inflows and density-driven currents, the hydrodynamics in South Bay are dominated by tides and wind waves and are weakly affected by stratification. The prevailing winds are dominated by a sea breeze from the west and northwest, reinforced by an inland movement of air caused by the solar heating in the Central Valley to the east. During the simulation period (9–26 September 2009), winds are strongest during the evening and calm at night.

3.4. Sensitivity to Sediment Model Setup

3.4.1. Micro/Macrofloc Ratio

We conduct sensitivity studies to understand how different values of $R_{m/M}$ on the shoals and channels affect model results. Unless otherwise noted, all sediment parameters are indicated in section 3.2, but with different values of $R_{m/M}$ on the channels and shoals. Time series of modeled SSC are obtained via interpolation to the

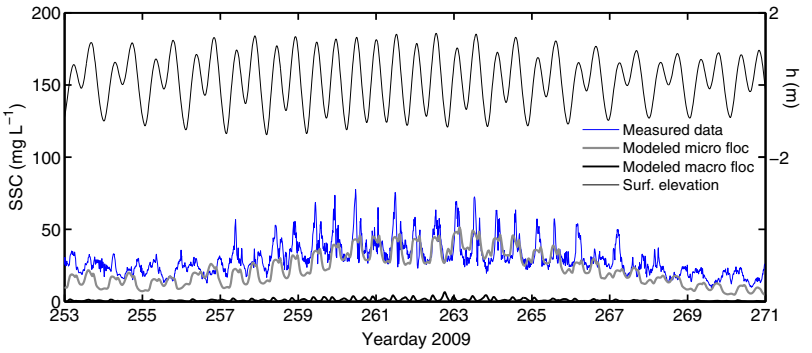

Figure 7. Modeled SSC related to macroflocs and microflocs for the base case (S05C43) compared to observations at the channel station. The modeled surface elevation is also shown for reference.

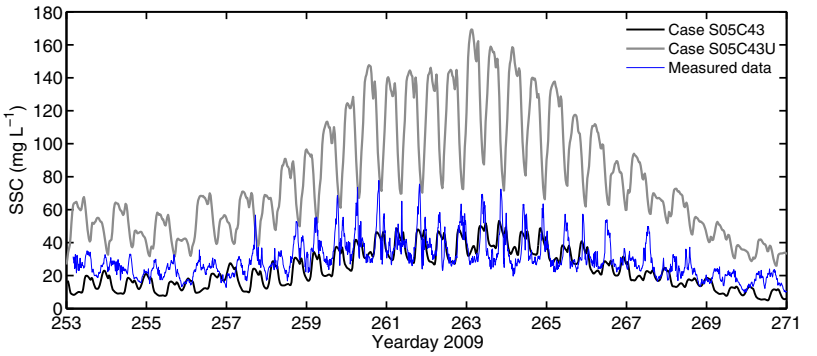

Figure 8. Comparison of modeled SSC at the channel station in the base case (S05C43) to the case in which the critical shear stress for the first bed layer is uniform throughout the domain (case S05C43U).

height of the instruments for comparison of the predictions to the observations. Simulations indicate that the best agreement between the model and observations occurs when $R_{m/M}=1/19 \approx 0.05$ on the shoals and $R_{m/M}=3/7 \approx 0.43$ in the channels. This is the base case and is used for further analysis of sediment transport

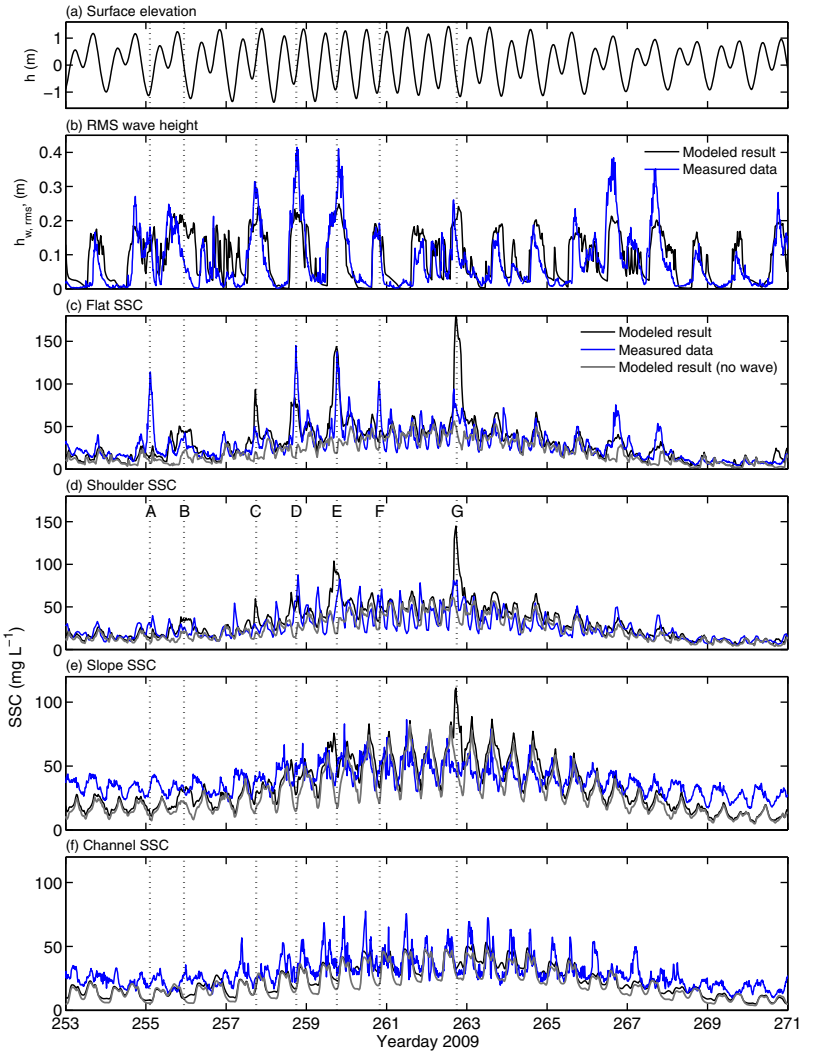

Figure 9. (a) Time series of modeled surface elevation, (b) RMS wave height at the flat station, (c) SSC at the flat station, (d) SSC at the shoulder station, (e) SSC at the slope station, and (f) SSC at the channel station. Vertical dotted lines highlight events A to G that are discussed in the text.

in the remainder of this study. In what follows, we adopt the convention that each case is named based on the two digit percentage of $R_{m/M}$ in the shoals and channels. For example, we refer to the base case as S05C43 (5% on the shoals and 43% in the channel). To demonstrate model sensitivity to $R_{m/M}$, four more cases are studied, as indicated in Table 3. Two are designed to understand the impact of changing $R_{m/M}$ on the shoals, namely cases S11C43 (more microfloc erosion on shoals) and S00C43 (less microfloc erosion on shoals), and two are designed to understand the impact of changing $R_{m/M}$ in the channels, namely cases S05C67 (more microfloc erosion in channels) and S05C25 (less microfloc erosion in channels). Five additional runs are indicated in Table 3, and these are designed to understand the impact of omitting the wave model (case S05C43NW) on the base case, the impact of omitting winds (case S05C43NWI), the shoal-channel exchange (cases SNRC43 and S05CNR), and the effects of assuming a spatially uniform bed-layer distribution (case S05C43U). Recall that, as discussed in section 3.2, the initial bed-layer thicknesses are based on the time-averaged bottom stress during the spin-up period. Assumption of a spatially uniform bed-layer thickness effectively amounts to a spatially uniform critical bottom stress for erosion.

To evaluate model accuracy, we use the skill score (*SS*) defined as (Wilmott, 1981)

$$SS = 1 - \frac{\sum |X_{mod} - X_{obs}|^2}{\sum \left(|X_{mod} - \overline{X}_{obs}| + |X_{obs} - \overline{X}_{obs}| \right)^2}, \tag{14}$$

where X_{mod} and X_{obs} are modeled and observed variables, respectively, and the overbar represents the mean value. Table 3 lists the Skill Score at the locations corresponding to the field observations (i.e., flat, shoulder, slope, and channel). It can be seen that the modeled SSC at the flat station is highly sensitive to $R_{m/M}$, i.e., an addition of a small amount of microflocs (i.e., 1−10%) can significantly improve the prediction. Time series of SSC corresponding to microflocs and macroflocs along with the observed time series of SSC and, for reference, time series of modeled surface elevation are shown in Figure 6 for the base case (S05C43). Due to the small settling velocity that leads to long settling times, the SSC related to microflocs follows the low-frequency variability of the tidal currents and can be thought of as a background field when compared to the SSC associated with macroflocs which have much shorter settling times. The result is SSC due to macroflocs that directly respond to tidal forcing with peaks during both flood and ebb tides and little to no suspension in between. The SSC due to microflocs varies more slowly and peaks intermittently during high-water slack tides. The combination of low-frequency and high-frequency SSC components is consistent with the finding of Brand et al. (2015) and demonstrates the fundamental feature of suspensions in South Bay in which the contribution from coarser sediments is due to local resuspension while that due to finer sediments is due to remote resuspension and transport. The result is total SSC (including both microflocs and macroflocs) that exhibits strong tidal asymmetry.

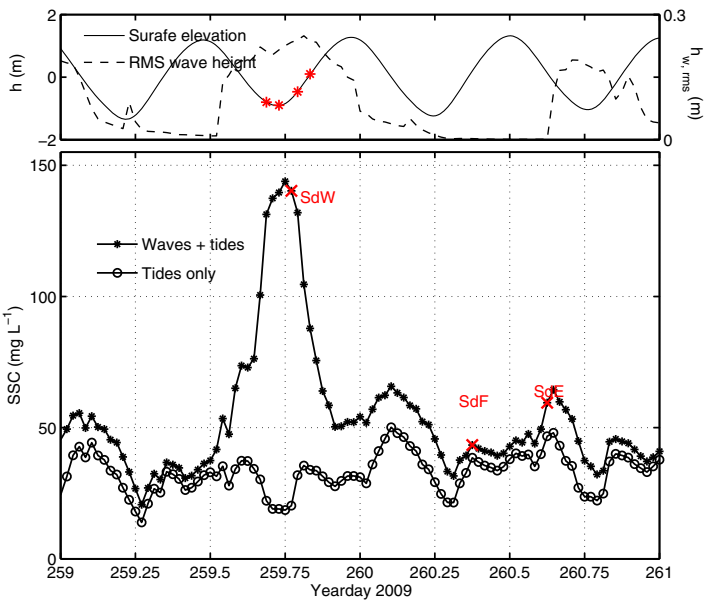

Figure 10. Zoomed-in view of Figure 9c showing the SSC at the flat station during yeardays 259–261 highlighting elevated SSC that occurs due to waves (SdW), flood tides (SdF), and ebb tides (SdE). The asterisks on the surface elevation curve correspond to the four representative time steps in Figure 12.

In contrast to the shallow-water shoal, the SSC in the deep water regions (stations channel and shoulder) shows little sensitivity to $R_{m/M}$. This can be seen from the comparison of skill scores for cases S05C43, S05C25, and S095C67 in Table 3. Similar to Figure 6, Figure 7 presents time series of SSC due to microflocs and macroflocs at the channel and shoulder stations, where it can be seen that microflocs dominate the SSC. In the deep water channel in lower South Bay, the resuspension is weak because of strong bed resistance to hydrodynamic forcing and most of the SSC arises from transport of microflocs from southern South Bay (discussed in section 4.3). This could also explain that when flows are energetic, such as in the deep water channel, flocs remain in the water column where they break up into microflocs. Combined with the finding of the dependence on $R_{m/M}$ in the shoal, the present model demonstrates a strong heterogeneity of micro/macrofloc fractions due to different suspension mechanisms in the shallow and deep water areas of South Bay.

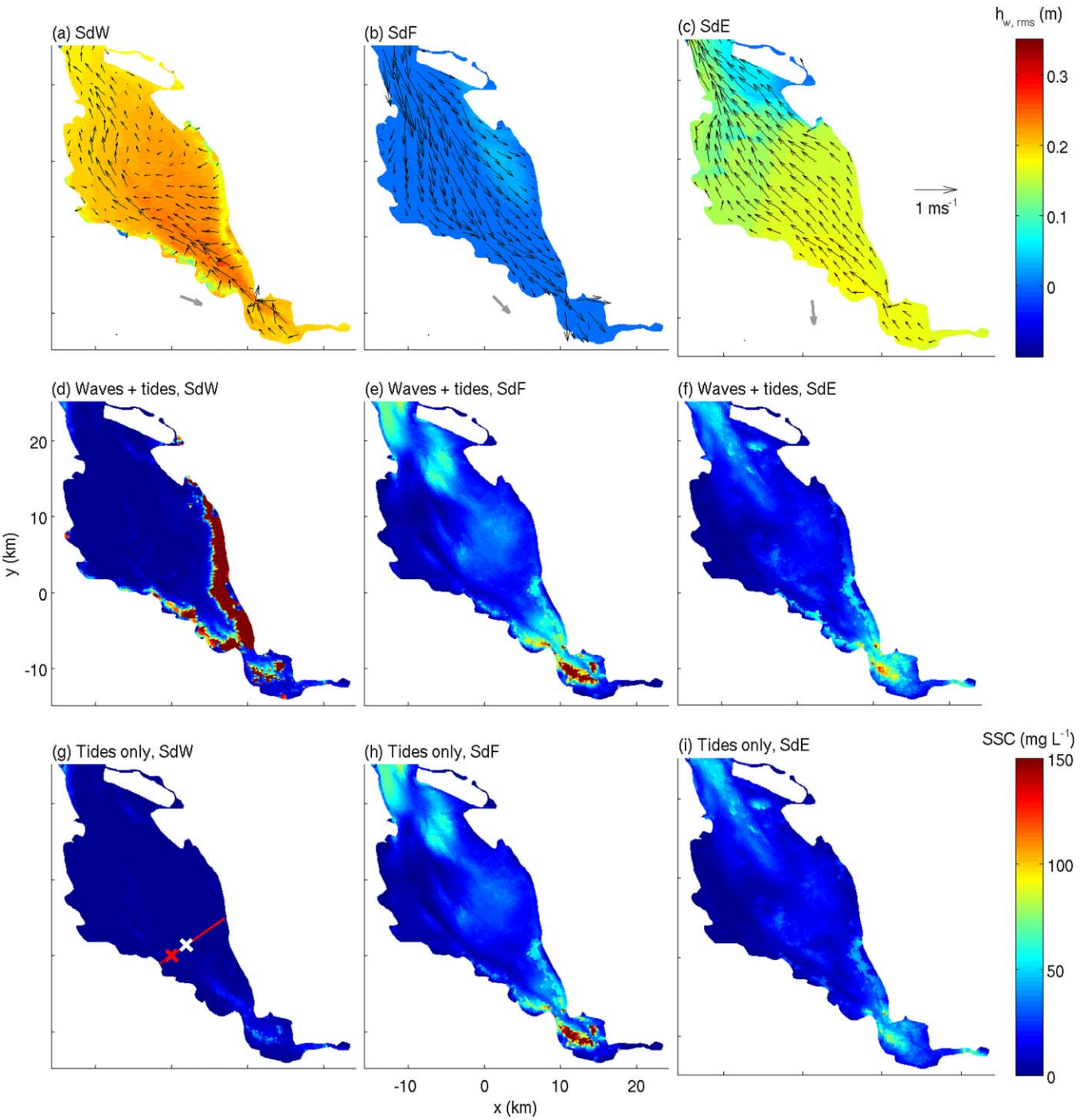

Figure 11. (top row) Snapshots of near-surface velocity vectors superimposed over contours of the wave height distribution and (middle row) the near-surface SSC predicted with and (bottom row) without waves, on 17 and 18 September 2009 (Yeardays 259–260). Each column of plots corresponds to the SSC during a wave event (SdW), a flood tide (SdF), and an ebb tide (SdE), as indicated in Figure 10. The crosses in plot (g) indicate the flat (white) and channel (red) measurement stations. The red solid line indicates the transect of SSC profiles presented in Figures 12 and 13. The gray arrows in plots (a–c) indicate the wind directions observed at the flat station. Wind speeds observed at the flat station are 6.72 m s^{-1} in SdW, 1.06 m s^{-1} in SdF, and 5.15 m s^{-1} in SdE.

3.4.2. Nonuniform Erosion

To demonstrate model sensitivity to the nonuniform bed erosion discussed in section 3.2, we compare the modeled SSC from the base case (S05C43) to the case in which the critical shear stress in the top layer is uniform throughout the domain (case S05C43U). As shown in Figure 8, in addition to the overprediction of

SSC due to the low bed resistance (small τ_{cr}) for case S05C43U, the SSC peaks have the wrong phase. This occurs because the small critical shear stress for erosion for case S05C43U leads to the predominance of bottom resuspension in the main channel, which results in two SSC peaks within a tidal cycle corresponding to flood and ebb tides, and low SSC during the high-water slacks. The SSC for case S05C43U also shows an important contribution of SSC at the channel station due to transport from the South, in that the SSC retains its high value during the ebb tide and does not agree with the field observations. For case S05C43, due to the greater critical shear stress for erosion in the deep water channel, bottom resuspension is weak and the primary SSC contribution is due to transport (discussed in section 4.3). As a result, the SSC peaks for the base case occur during high-water slack tides and are weakest during low-water slacks, which is consistent with the field observations. Table 3 also shows a good skill score for case S05C43 and a poor skill score for case S05C43U. In addition to demonstrating the importance of nonuniform bed resistance on accurate prediction of SSC in a complex estuarine setting, these results demonstrate that, unlike the shallow-water shoals in which the SSC is due to both bottom resuspension and transport, transport of sediment from southern South Bay is the dominant mechanism responsible for SSC in the deep water channel in South Bay.

4. Results and Discussion

4.1. Effects of Tides and Waves at the Location of the Field Observations

Figure 9 presents time series of observed and modeled surface elevation, root mean squared wave height, and SSC on the shoal and channel for the base case (S05C43). Plots c and d demonstrate good overall agreement between observed and predicted SSC on the shoal and in the channel, respectively, given that $SS = 0.75$ at the flat location and 0.81 at the channel location (Table 3). Because both simulated tides and waves have been validated in Chou et al. (2015), here we focus on the influence of these effects on SSC. In Figure 9, we highlight seven events associated with spikes of high SSC, indicated by letters A through G. These include spikes in SSC that are either predicted by the model or observed in the field. To demonstrate the effects of waves, model results of SSC without the wave model are also shown. Figure 9b shows that there were three strong wave events in the afternoons of yeardays 257–259 (events C, D, and E). These three events occurred during the start of flood tides following low water, indicating that the events of high SSC on the shoal (Figure 9c) occur because of wind-driven resuspension rather than tidal currents. This highlights the need to include the wave-driven stress and the subsequent resuspension in the model to obtain reasonable predictions of these SSC peaks, for which the predicted wave-induced SSC on the shoals is roughly 4–5 times larger than that driven by tides alone.

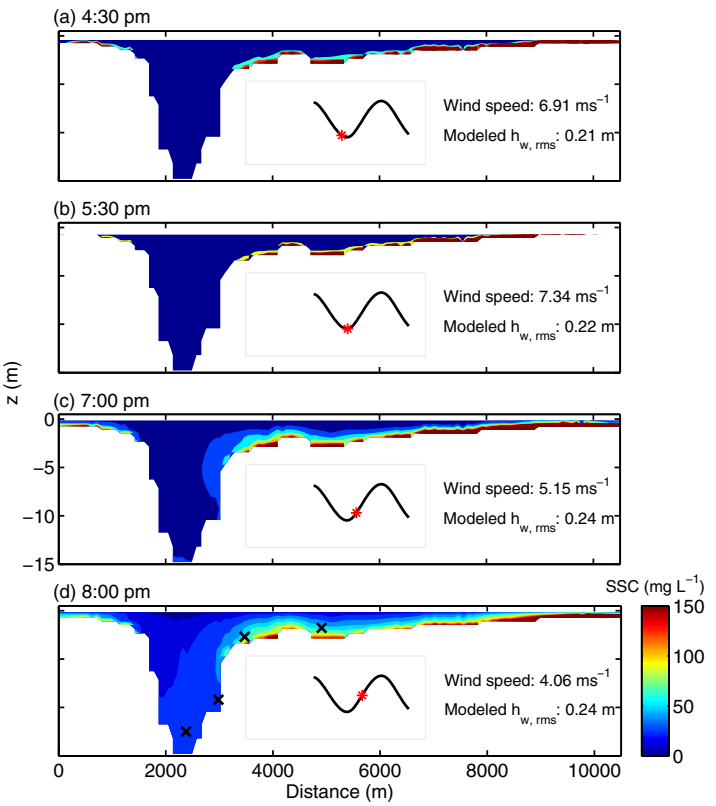

Figure 12. Modeled SSC along the transect shown in Figure 11f at four representative time steps during a wind event on 17 September 2009 (Yearday 259) (see Figure 10, indicated by asterisks). The crosses in plot (d) indicate the locations of measurement at (from right to left) the flat, shoulder, slope, and channel stations.

Discrepancies between modeled and predicted results on the shoals are found during events A, B, F, and G. The overprediction of SSC during events B and G on the shoals arises from the overprediction of the duration of peak wave events rather than an incorrect prediction of wind-wave amplitudes. As shown in Figure 9b, wave amplitudes are reasonably predicted during events B and G, although the wave events last too long, particularly during event B. This occurs because the mud layer in the model (i.e., the top two layers in the three-layer bed mud model) may not provide sufficient dissipation to attenuate waves. Furthermore, as noted in Chou et al. (2015), inaccurate predictions of the wave field may be due to inaccurate predictions of local winds which are smoothed in space by the spatial interpolation of the limited number of wind stations in the region. The delayed reduction of SSC after a strong resuspension event may also arise from the lack of flocculation physics in our model which would lead to faster settling of sediments that flocculate after a strong wind-driven

resuspension event. Flocculation may be even more prevalent during events B and G which occur close to slack tides when breakup mechanisms arising from strong tidally driven turbulence that may break up flocs are weak. Correctly including bottom mud layer effects and flocculation/breakup physics are subjects of active research in sediment transport modeling (e.g., Sheremet et al., 2011; Son & Hsu, 2011). During events A and F, because both the model prediction and field measurement show relatively weak waves compared to events C, D, and E, the under-prediction of SSC on the shoals could be due to insufficient parameterization for complex suspension processes. Because events A and F occurred during flood following slack tide, the model may under-predict the SSC because of the lack of turbulence-induced breakup which would produce more microflocs and delay deposition.

Despite the lack of wave-driven resuspension in the channel owing to its depth, Figure 9d shows that there is substantially more SSC in the channel when the wave model is turned on. We attribute this to wave-induced suspension on the shoal and subsequent transport into the channel, as discussed in section 4.3. As the water column becomes deeper, microflocs remain in suspension for longer and flocculation and turbulence-induced break up may impact sedimentation and resuspension processes, thus leading to variable floc sizes in time. While these effects are not taken into account in the present model, floc interactions in the field contribute to model uncertainty, making the prediction of SSC in the deep water channel more difficult than in the shoal. This is evidenced by the fact that the model consistently underestimates SSC in the channel during spring tides.

4.2. Spatial Distribution of SSC

To examine different suspension mechanisms induced by waves and tides, we focus on three SSC events at the flat station, indicated by SdW, SdF, and SdE in Figure 10, which is a zoomed-in view of Figure 9c. Event SdW represents a typical case of suspension induced by a strong wave event, while events SdF and SdE represent tide-induced suspensions due to flood and ebb tidal currents, respectively. Snapshots of flow velocity vectors superimposed over the wave height distributions as well as the resulting SSC distributions in South Bay during these three representative events are shown in Figure 11. Velocity and SSC shown in Figure 11 are model results in a horizontal plane located 0.74 m below mean sea level. The spatial distributions of SSC during these three events are described in detail below.

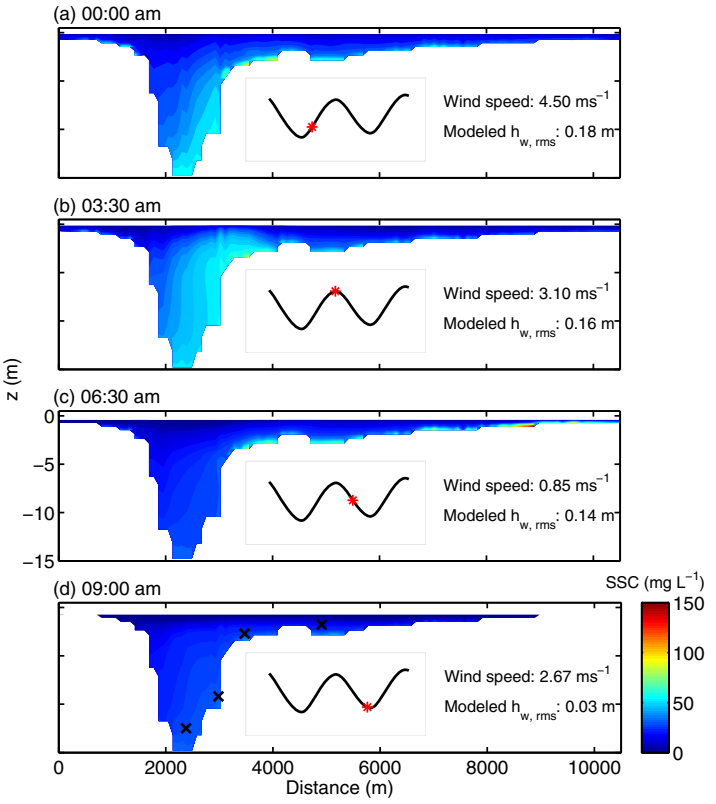

Figure 13. Snapshots of modeled SSC along the transect shown in Figure 11f during a semidiurnal tidal cycle on 19 September 2009 (Yearday 262). The crosses in plot (d) indicate the locations of measurement at (from right to left) the flat, shoulder, slope, and channel stations.

4.2.1. Wave-Induced Suspension

Comparing Figures 11d–11g highlights the modeled wave-induced suspension in the shallow-water regions during a strong-wind event. In the model, the dominant wave length during the wind event ranges from 4 to 6 m. Therefore, based on linear wave theory, only beds in the regions where the depth is less than 4 m are influenced by waves. Figure 11d shows that a significant amount of suspension is induced by wind waves where the depth is less than 4 m. Wind waves are the main source of suspensions in shallow-water regions along the shoreline ($d \approx 1$ m) owing to the dominance of wave-driven stresses over those due to the tidal currents (see Figure 11g).

We further examine the wave-induced suspension by plotting vertical profiles along the transect shown in Figure 11g, which passes through the measurement sites described in section 3.3. Figure 12 shows a series of hourly snapshots of SSC profiles in response to strong-wind waves during event SdW marked in Figure 10. It can be seen that waves begin to induce strong bed stresses during the early stages of wave development, resulting in high near-bed SSC on the shoals (see Figures 12a and 12b). As the water depth becomes shallower at the end of the ebb tide, larger wave-induced shear stresses are exerted on the bed and these induce greater near-bed suspensions, especially during slack tides (see Figure 12b). However, because of low flow energetics (i.e., weak turbulence) during the slack tide, suspended sediment is confined to a very thin near-bed region, leading to a sharp

near-bed concentration gradient, as shown in Figures 12 a through c. Following the strong turbulence and vertical mixing induced by the succeeding flood tide, newly eroded sediments are quickly suspended into the water column (see Figure 12d). Based on the behavior highlighted above, wind waves act as a stirring mechanism that induces initial suspension of bottom mud on the shoals. In the absence of strong currents, the excited suspended mud is confined to a region near the bed which is susceptible to rapid settling without persistent wave forcing. The bottom mud on the shoals can be further suspended into the water column only if tidal currents following wave events are sufficiently strong. This effect is the main mechanism resulting in wave-induced SSC peaks at the flat station during yeardays 257 through 259, as marked with C, D, and E in Figure 9.

4.2.2. Tidal Suspension

Comparison of tidal suspensions during flood and ebb tides (see Figures 11e, 11f, 11h, and 11i) shows that the currents during flood tides are usually stronger than those during ebbs, resulting in much stronger suspension in the lower South Bay and an additional SSC patch in the middle of South Bay (see Figures 11h and 11i) during the flood tide. Tidal suspensions are further examined by plotting vertical profiles along the transect shown in Figure 11g. Figure 13 shows SSC profiles in response to a typical tidal current at four representative instants in time during a semidiurnal tidal cycle. The dominant effect of the tides is to promote suspensions in the deep channel, and sediment remains suspended for longer than in the shallow-water shoals. Within a tidal cycle, the largest SSC occurs during the flood tide when bottom stresses and turbulence intensities are strongest. Owing to the delayed settling in the channel and the elevated effects of turbulence and mixing, SSC in deep channels usually exhibits less temporal variability when compared to SSC behavior on the shoals, which respond more rapidly to intermittent wind-wave events.

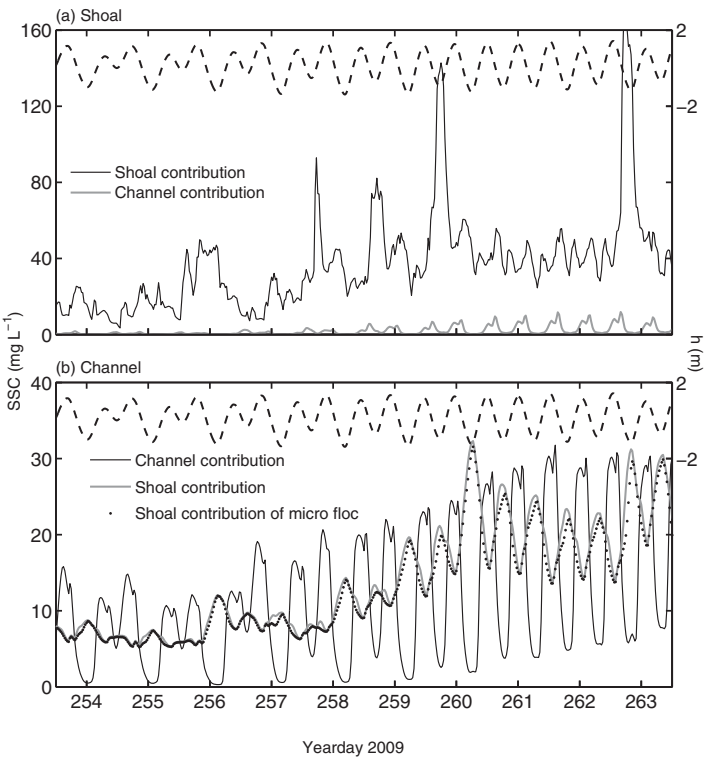

Figure 14. Time series of SSC (a) at the flat station due to suspension in the shoal obtained from the difference between SSC for case S05C43 and that for case SNRC43, which has no erosion in the shoals (black line), and the contribution from the channel obtained from case SNRC43 (gray line) and (b) at the channel station due to suspension in the channel obtained from the difference between SSC for case S05C43 and that for case S05CNR, which has no erosion in the channels (black line), and the contribution from the shoals obtained from S05CNR (gray line).

4.3. Shoal-Channel Exchange

4.3.1. Shoal/Channel SSC Contributions at the Location of the Field Observations

To evaluate the contributions to the SSC arising from shoal-channel exchange, we study two additional cases. In the first case, we eliminate erosion of sediments from the bed in channel regions by setting $E_{b,q}=0$ for water depths exceeding 5 m, denoted as case S05CNR. In the second case, we eliminate erosion on the shoals by setting $E_{b,q}=0$ for water depths less than 5 m, denoted as case SNRC43. The SSC result in the channel for case S05CNR indicates the shoal contribution to the SSC in the channel and in case SNRC43 indicates the channel contribution to the shoal. An estimate of SSC in the channel that arises from transport in the channel and local suspension can thus be obtained by subtracting the SSC in case S05CNR from the result for case S05C43. The same can be done in the shoals by subtracting the SSC in case SNRC43 from the SSC for case S05C43 to indicate the contribution in the shoal in the absence of advection from the channel. As shown in Figure 14a, the contribution of advection from the channels on the SSC at the shoal station (SSC from case SNRC43) is much smaller than that due to local suspension and advection (given by SSC[case S05C43]–SSC[case SNRC43]). The localized behavior of SSC on the shoals arises from the low-water depths and relatively weak tidal flow energetics that result in short residence times of suspended sediments. As a result, transport distances of suspended sediments are relatively short, and vertical resuspension and local transport are the dominant sources of SSC on the shoals. In contrast to the behavior at the flat station, Figure 14b shows that in the channel, the contribution to the SSC from the shoals (SSC from S05CNR) is roughly the same as the local contribution (given by SSC[case S05C43]–SSC[case S05CNR]).

As indicated by the water surface elevation in Figure 14b, the contribution to the SSC from the shoals in the channel typically increases

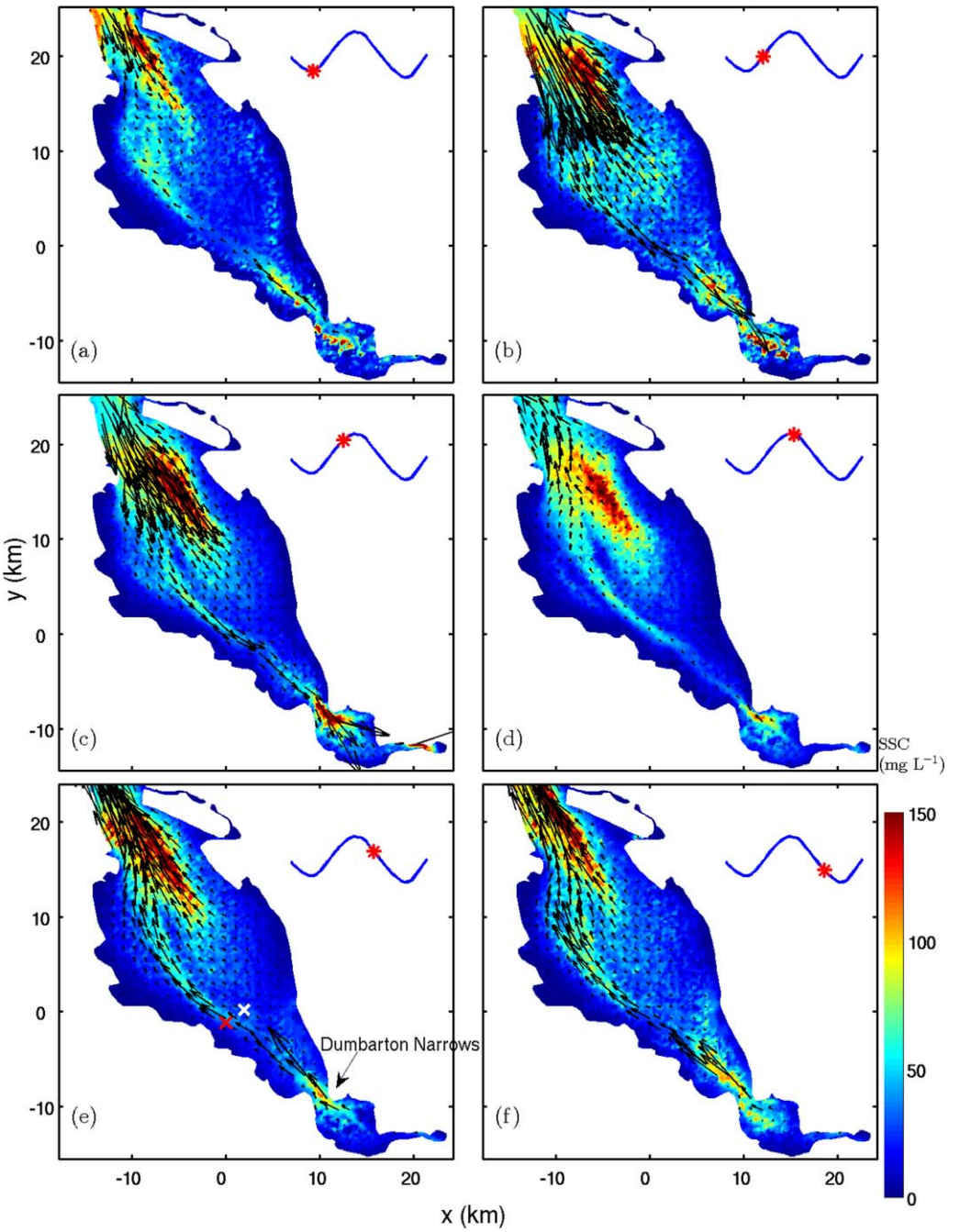

Figure 15. Snapshots of depth-integrated sediment fluxes (black arrows) superimposed over depth-averaged SSC over a tidal cycle starting from the second low-water slack tide on 17 September 2009 (Yearday 259). The crosses in plot (e) indicate the flat (white) and channel (red) measurement stations.

during the ebb tides and reaches its maximum during low-water slack (e.g., Yearday 256) and then decreases. This is in contrast to the channel contribution, which typically peaks twice during peak flood and ebb tides. As shown in Figure 14b, most of these sediments are microflocs, which are associated with a longer residence time in the water column and therefore can be transported over longer distances.

4.3.2. Tidal SSC Flux

To examine the mechanism driving sediments from the shoals into the channels, we analyze spatial distributions of the depth-averaged SSC, which we denote $\overline{C}$, and the depth-integrated suspended sediment flux, which is given by

$$\mathbf{F} = \int_{-d}^{h} \mathbf{u}_H C_{total}\, dz\,, \tag{15}$$

where d is the depth, h is the free-surface height, $\mathbf{u}_H$ is the horizontal velocity vector, and C_{total} is the total SSC defined in equation (2). These are indicated at different points in time over a tidal cycle beginning at the second low-water slack tide on yearday 259 in Figure 15. As the depth increases, the flow becomes more energetic, thus enhancing both SSC and fluxes. The largest fluxes occur at the north boundary, indicating significant exchange between Central Bay and South Bay. The fluxes reach peak values during peak ebb and flood tides (see Figures 15b and 15e) and are negligible during slack water (see Figures 15a and 15d).

Despite the time series in Figure 14 that clearly indicate the contribution from the shoals to the SSC in the main channel at the observation sites, there are no clear cross-channel fluxes of sediment throughout most of South Bay in Figure 15 during a typical tidal event. However, it is clear that the high concentrations of SSC occur at the end of the flood tide in the Dumbarton Narrows. If local resuspension is responsible for this high SSC, then we would expect to have equally high values of SSC in the Dumbarton Narrows at the end of the ebb tide because the flood and ebb currents are roughly equal at this location. However, the SSC at or near the end of the ebb tide (Figures 15a and 15f) is significantly lower than it is at the end of the flood tide (Figure 15c). Rather than due solely to local resuspension, a large fraction of the SSC at the Dumbarton Narrows is due to transport from the shoals. This transport is due to convergence of the southward depth-integrated fluxes on the shoals due to the lateral contraction of the South Bay shoreline at the Narrows. After high SSC is created in this region at the end of the flood tide, northward flows by the subsequent ebb tide transport the sediment to the north and across the measurement stations, as indicated by the strong northward depth-integrated sediment fluxes in the main channel. This transport pathway is the most plausible explanation for why the contribution to the SSC from the shoals in the channel is a maximum at the end of the ebb tide in Figure 14. Because it is locally derived, the contribution from the channel itself peaks twice around high water during the flood and ebb tides.

4.3.3. Wind-Induced SSC Flux

In addition to the aforementioned tide-driven shoal-channel exchange due to the lateral contraction of the shoreline at southern South Bay, the action of winds can also enhance shoal-channel exchange of suspended sediments. Figure 16 shows the depth-integrated SSC fluxes superimposed over the surface elevation for the base case (S05C43) and the case without wind (case S05C43NWI), i.e., no wind waves and no

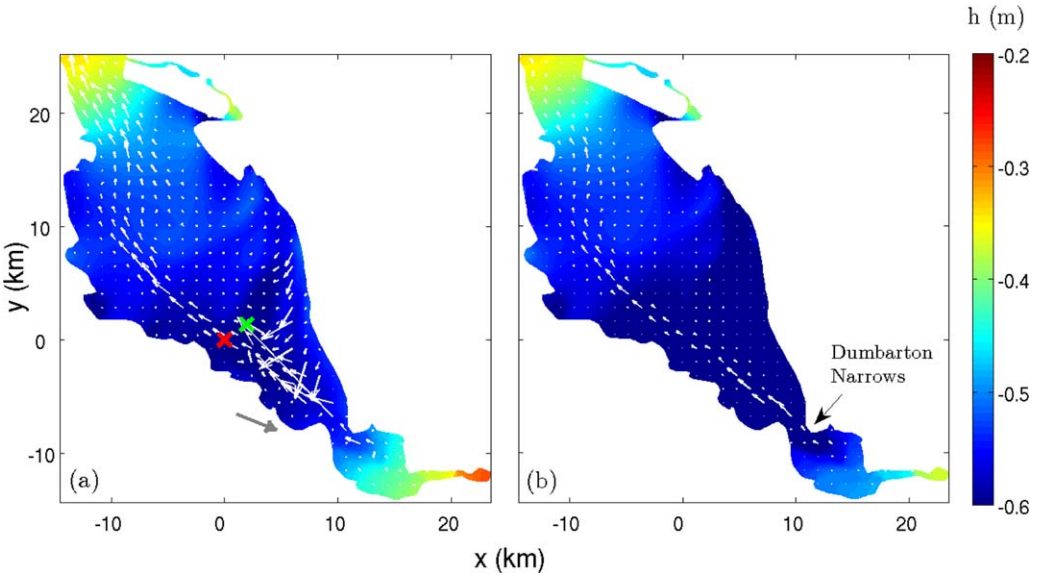

Figure 16. Snapshots of depth-integrated sediment fluxes (white arrows) superimposed over the free surface during a wave event (SdW), as indicated in Figure 10, for (a) the base case (S05C43) and (b) the case without wind (S05C43NWI). The crosses in plot (c) indicate the flat (green) and channel (red) measurement stations. The gray arrow in Figure 16a indicates the wind direction. The wind speed is roughly uniform in the region with a magnitude of 7 m s^{-1}.

wind-driven currents. The results show that a wind event occurring during low water at the end of an ebb tide significantly enhances cross-channel sediment fluxes. This is mainly due to strong bottom orbital velocities induced by wind waves in the shallow-water regions, leading to strong sediment resuspension, which is evident when comparing the SSC on the shoals with and without the effect of wind-waves in Figures 11d and 11g, respectively. This results in considerable sediment flux toward the channel from the shoals, as shown in Figures 16a. Also, persistent westerly to northwesterly winds (see Figure 16a) drive surface currents to the southeast, resulting in currents toward the channel due to contraction, which can also enhance shoal-channel exchange of suspended sediment.

5. Summary and Conclusions

We have presented a three-dimensional sediment transport model to study suspended sediment transport in complex estuarine settings. The model is composed of a multiclass advection-diffusion equation that models transport of two classes of fine suspensions and a multilayer bed model to parameterize complex bed-sediment processes. The suspended sediment and bed models are incorporated into a coupled wave-hydrodynamics model, thereby enabling prediction of sediment resuspension and transport in response to both waves and tidal currents. Although the model has the capability to compute morphological effects, the time scales simulated in the present paper are short and so morphological effects are assumed not to be significant.

The model is applied to study sediment transport in South Bay, and the results are validated with observations along a cross-channel transect that covers the deep channel, side slope of the channel, and shallow-water shoal. Our focus is on the effect of nonuniform erosion and the ratio of microflocs to macroflocs, $R_{m/M}$, that are resuspended from the bed. Using a value of $R_{m/M}=1/19$, we obtain skill score values that are higher than typical skill scores for SSC modeling reported in the literature. The results at the flat station show that SSC related to macroflocs is a result of the direct response to tidal forcing (i.e., local resuspension) while SSC related to microflocs is primarily due to transport, leading to tidal asymmetry of total SSC. Moreover, we show that it is necessary to consider nonuniform distribution of the critical shear stress for erosion. This is especially important in the deep water channel where the flow is energetic and high shear stresses prevent the formation of a fluff layer, thus leading to a bed that should be more resistant to bottom shear stresses. The effect is a channel in which a large fraction of the SSC is derived from nonlocal transport rather than local resuspension.

Comparison of model results obtained with and without waves demonstrates the significance of wave-induced suspension. While strong winds lead to resuspension on the shoals, sediment resuspended by wind-waves remains in a near-bed layer unless tidally driven turbulence mixes it throughout the water column. In the present study, it is thus only the combination of wind-waves and tidal currents that leads to the observed high SSC.

Numerical tests show that the SSC at the channel station has a significant contribution due to advection from the shoals. The spatial distribution of depth-integrated sediment fluxes shows no clear cross-channel fluxes throughout most of South Bay. However, lateral contraction of the shoreline at the Dumbarton Narrows drives sediment that is resuspended during the flood tide southward along the shoals into the channel at the Narrows. This sediment is then transported to the north and across the observation stations in the channel during the subsequent ebb tide. This explains how the contribution to SSC in the channel from the shoals peaks during low slack after ebb and is out of phase with the local resuspension, which peaks twice during both flood and ebb tides.

Acknowledgments
The project was supported by a grant from the California State Coastal Conservancy. Y. J. C. thanks Dave Schoellhamer for his helpful suggestions at the beginning stage of the project, which guided the development of the present two-size sediment transport model. Simulations were carried out using supercomputers at the Peter A. McCuen Environmental Computing Center at Stanford University and at Taida Institute of Mathematical Science (TIMS) at National Taiwan University. All the data and simulation code necessary to reproduce the results in the present study can be obtained at http://web.stanford.edu/group/suntans/data/chou-etal-jgr-2018.

References

Bever, A. J., & MacWilliams, M. L. (2013). Simulating sediment transport processes in San Pablo Bay using coupled hydrodynamic, wave, and sediment transport models. *Marine Geology*, *345*, 235–253.

Blumberg, A. F., Galperin, B., & O'connor, D. J. (1992). Modeling vertical structure of open-channel flow. *Journal of Hydraulic Engineering*, *118*, 1119–1134.

Blumberg, A. F., & Mellor, G. L. (1987). A description of a three-dimensional coastal ocean circulation model. In N. Heaps (Ed.), *Three-dimensional coastal ocean models* (pp. 1–16). Washington, DC: American Geophysical Union.

Bonaldo, D., Benetazzo, A., Sclavo, M., & Carniel, S. (2015). Modelling wave-driven sediment transport in a changing climate: A case study for northern Adriatic Sea (Italy). *Regional Environmental Change*, *15*, 45–55.

Booij, N., Ris, R. C., & Holthuijsen, L. H. (1999). A third generation wave model for coastal regions. 1: Model description and validation. *Journal of Geophysical Research*, *104*(C4), 7649–7666.
Brand, A., Lacy, J. R., Gladding, S., Holleman, R., & Stacey, M. (2015). Model-based interpretation of sediment concentration and vertical flux measurements in a shallow estuarine environment. *Limnology and Oceanography Methods*, *60*, 463–481.
Brand, A., Lacy, J. R., Hsu, K., Hoover, D., Gladding, S., & Stacey, M. T. (2010). Wind-enhanced resuspension in the shallow waters of South San Francisco Bay: Mechanisms and potential implications for cohesive sediment transport. *Journal of Geophysical Research*, *115*, C11024. https://doi.org/10.1029/2010JC006172
California Department of Water Resources (CDWR) (1986). *DAYFLOW program documentation and data summary user's guide* (technical report). Sacramento, CA: California Department of Water Resources.
Carniel, S., Bonaldo, D., Benetazzo, A., Bergamasco, A., Boldrin, A., Falcieri, F. M., et al. (2016). Off-shelf fluxes across the southern Adriatic margin: Factors controlling dense-water-driven transport phenomena. *Marine Geology*, *375*, 44–63.
Carniello, L., Defina, A., Fagherazzi, S., & D'alpaos, L. (2005). A combined wind wave-tidal model for the Venice Lagoon, Italy. *Journal of Geophysical Research*, *110*, F04007. https://doi.org/10.1029/2004JF000232
Chen, C., Liu, H., & Beardsley, R. C. (2003). An unstructured finite volume, three-dimensional primitive equation ocean model: Application coastal ocean and estuaries. *Journal of Atmospheric and Oceanic Technology*, *20*, 159–186.
Chou, Y.-J., Holleman, R. C., Fringer, O. B., Stacey, M. T., Koseff, J. R., & Monismith, S. G. (2015). Three-dimensional wave-coupled hydrodynamic modeling in South San Francisco Bay. *Computers & Geosciences*, *85*, 10–21.
Chua, V. P., & Fringer, O. B. (2011). Sensitivity analysis of three-dimensional salinity simulations in North San Francisco Bay using the unstructured-grid SUNTANS model. *Ocean Modelling*, *39*, 332–350.
Cloern, J. E. (1987). Turbidity as a control on phytoplankton biomass and productivity in estuaries. *Continental Shelf Research*, *7*(11–12), 1367–1381.
Collignon, A. G., & Stacey, M. T. (2012). Intratidal dynamics of fronts and lateral circulation at the shoal-channel interface in a partially stratified estuary. *Journal of Physical Oceanography*, *42*(5), 869–883.
Collignon, A. G., & Stacey, M. T. (2013). Turbulence dynamics at the shoal-channel interface in a partially stratified estuary. *Journal of Physical Oceanography*, *43*(5), 970–989.
Deltares (2018a). *Delft3d-flow user manual*. Delft, the Netherlands: Deltares.
Deltares (2018b). *D-flow flexible mesh*. Delft, the Netherlands: Deltares.
DHI (2007). *MIKE 21 flow model: Mud transport module. User guide*. Horsholm, Denmark: DHI Water and Environment.
Dyer, K. R., & Soulsby, R. L. (1988). Sand transport on the continental shelf. *Annual Review of Fluid Mechanics*, *20*, 295–324.
Fringer, O. B., Gerritsen, M., & Street, R. L. (2006). An unstructured-grid finite volume, nonhydrostatic, parallel coastal ocean simulator. *Ocean Modelling*, *14*, 139–173.
Ganju, N. K., Schoellhamer, D. H., & Jaffe, B. E. (2009). Hindcasting of decadal-timescale estuarine bathymetric change with a tidal-timescale model. *Journal of Geophysical Research*, *114*, F04019. https://doi.org/10.1029/2008JF001191
Gessler, D., Hall, B., Spasojevic, M., Holly, F., Pourtaheri, H., & Raphelt, N. (1999). Application of a 3D mobile bed, hydrodynamic model. *Journal of Hydraulic Engineering*, *125*(7), 737–749.
Grant, W. D., & Madsen, O. S. (1986). The continental-shelf bottom boundary layer. *Annual Review of Fluid Mechanics*, *18*, 265–305.
Gross, E. S., MacWilliams, M. L., & Kimmerer, W. (2005). Simulating periodic stratification in the San Francisco Estuary. In *Proceedings of the 9th international conference on estuarine and coastal modelling, ASCE conference proceedings* (pp. 155–175). Reston, VA: American Society of Civil Engineers (ASCE).
Haas, K. A., & Warner, J. C. (2009). Comparing a quasi-3D to a full 3D nearshore circulation model: SHORECIRC and ROMS. *Ocean Modelling*, *26*, 91–103.
Harris, C. K., Sherwood, C. R., Signell, R. P., Bever, A. J., & Warner, J. C. (2008). Sediment dispersal in the northwestern Adriatic Sea. *Journal of Geophysical Research*, *113*, C11S03. https://doi.org/10.1029/2006JC003868
Higgins, S. A., Jaffe, B. E., & Fuller, C. C. (2007). Reconstructing sediment age profiles from historical bathymetry changes in San Pablo Bay, California. *Estuarine, Coastal and Shelf Science*, *73*(1–2), 165–174.
Huang, Y., Weisberg, R. H., & Zheng, L. (2010). Coupling of surge and waves for an Ivan-like hurricane impacting the Tampa Bay, Florida region. *Journal of Geophysical Research*, *115*, C12009. https://doi.org/10.1029/2009JC006090
Jaffe, B. E., Smith, R. E., & Foxgrover, A. C. (2007). Anthropogenic influence on sedimentation and intertidal mudflat change in San Pable Bay, california. *Estuarine, Coastal and Shelf Science*, *73*(1–2), 175–187.
Kranenburg, C. (1994). On the fractal structure of cohesive sediment aggregates. *Estuarine, Coastal and Shelf Science*, *39*, 451–460.
Lacy, J. R., Gladding, S., Brand, A., Collignon, A., & Stacey, M. (2014). Lateral baroclinic forcing enhances sediment transport from shallows to channel in an estuary, *Estuaries and Coasts*, *37*, 1058–1077. https://doi.org/10.1007/s12237-013-9748-3
Lacy, J. R., Schoellhamer, D. H., & Burau, J. R. (1996). Suspended-solids flux at a shallow-water site in South San Francisco Bay. In *Proceedings of the North American water and environment congress*. New York, NY: American Society of Civil Engineers.
Lee, V., Mineart, P., & Armstrong, L. (2004). Calibration of a sediment transport model for San Francisco Bay. In *Proceedings of 8th international conference on estuarine and coastal modeling* (pp. 1007–1026). Reston, VA: American Society of Civil Engineers (ASCE).
Lick, W. (2009). *Sediment and contaminant transport in surface waters* (400 p.). Boca Raton, FL: CRC Press.
Lick, W., Lick, J., & Ziegler, C. K. (1992). Flocculation and its effect on the vertical transport of fine-grained sediments. *Hydrobiologia*, *235/236*, 1–16.
Lumborg, U., & Pejrup, M. (2005). Modelling of cohesive sediment transport in a tidal lagoon—An annual budget. *Marine Geology*, *218*, 1–16.
MacVean, L. J., & Lacy, J. R. (2014). Interactions between waves, sediment, and turbulence on a shallow estuarine mudflat. *Journal of Geophysical Research*, *119*, 1534–1553. https://doi.org/10.1002/2013JC009477
Manning, A. J., & Schoellhamer, D. H. (2013). Factors controlling floc settling velocity along a longitudinal estuarine transect. *Marine Geology*, *345*, 266–280.
McKee, L. J., Ganju, N. K., & Schoellhamer, D. H. (2006). Estimates of suspended sediment entering San Francisco Bay from Sacramento and San Joaquin Delta, San Francisco Bay, California. *Journal of Hydrology*, *323*(1–4), 335–352.
Mellor, G. L., & Yamada, T. (1982). Development of a turbulence closure model for geophysical fluid problem. *Reviews of Geophysics and Space Physics*, *20*, 851–875.
Mikeš, D., & Manning, A. J. (2010). Assessment of flocculation kinetics of cohesive sediments from the Seine and Gironde estuaries, France, through laboratory and field studies. *Journal of Waterway, Port, Coastal, and Ocean Engineering*, *136*(6), 306–318.
Nielsen, P., & Teakle, I. A. L. (2004). Turbulent diffusion of momentum and suspended particles: A finite mixing length theory. *Physics of Fluids*, *16*(7), 2342–2348.

Parchure, T. M., & Mehta, A. J. (1985). Erosion of soft cohesive sediment deposits. *Journal of Hydraulic Engineering*, *111*(10), 1308–1326.
Richardson, J. F., & Zaki, W. N. (1954). The sedimentation of a suspension of uniform spheres under conditions of viscous floc. *Chemical Engineering Science*, *3*, 65–73.
Rodi, W. (1984). *Turbulence models and their application in hydraulics: A state of the art review* (technical report). Delft, the Netherlands: International of Association for Hydraulics Research.
Roelvink, J. A. (2006). Coastal morphodynamic evolution techniques. *Coastal Engineering*, *53*, 277–287.
Sanford, L. P., & Maa, J. P. (2001). A unified erosion formulation for fine sediments. *Marine Geology*, *179*, 9–23.
Schoellhamer, D. H. (1996). Factors affecting suspended-solids concentrations in South San Francisco Bay, California. *Journal of Geophysical Research*, *101*(C5), 12089–12095.
Scott, K. J. (1984). *Hindered settling of a suspension of spheres; critical evaluation of equations relating settling rate to mean particle diameter and suspension concentration* (Rep. CENG 497). South Africa: CSIR, Chemical Engineering Research Group
Shchepetkin, A. F., & McWilliams, J. (2005). The regional oceanic modeling system: A split-explicit, free-surface, topography-following-coordinate ocean model. *Ocean Modelling*, *9*, 347–404.
Sheng, Y. P., & Liu, T. (2011). Three-dimensional simulation of wave-induced circulation: Comparison of three radiation stress formulations. *Journal of Geophysical Research*, *116*, C05021. https://doi.org/10.1029/2010JC006765
Sheremet, A., Jaramillo, S., Su, S.-F., Allison, M. A., & Holland, K. T. (2011). Wave-mud interaction over the muddy Atchafalaya subaqueous clinoform, Louisiana, United States: Wave processes. *Journal of Geophysical Research*, *116*, C06005. https://doi.org/10.1029/2010JC006644
Son, M., & Hsu, T. (2011). The effects of flocculation and bed erodibility on modeling cohesive sediment resuspension. *Journal of Geophysical Research*, *116*, C03021. https://doi.org/10.1029/2010JC006352
Sterling, M. C., Bornner, J. S., Ernest, A. N. S., Page, C. A., & Autenrieth, R. L. (2005). Application of fractal flocculation and vertical transport model to aquatic sol-sediment systems. *Water Research*, *39*, 1818–1830.
Umlauf, L., & Burchard, H. (2003). A generic length-scale equation for geophysical turbulence models. *Journal of Marine Research*, *61*, 235–265.
van der Wegen, M., Dastgheib, A., Jaffe, B. E., & Roelvink, D. (2011a). Bed composition generation for morphodynamic modeling: Case study of San Pablo Bay in California, USA. *Ocean Dynamics*, *61*, 173–186.
van der Wegen, M., Dastgheib, A., Jaffe, B. E., & Roelvink, D. (2011b). Process-based, morphodynamic hindcast of decadal deposition patterns in San Pablo Bay, California, USA. *Ocean Dynamics*, *61*, 173–186.
van Rijn, L. C. (1984). Sediment transport. Part 2: Suspended load transport. *Journal of Hydraulic Engineering*, *110*(11), 1613–1642.
Walters, R. A., Cheng, R. T., & Conomos, T. J. (1985). Time scales of circulation and mixing processes of San Francisco Bay waters. *Hydrobiologia*, *129*, 13–36.
Warner, J. C., Armstrong, B., He, R., & Zambon, J. B. (2010). Development of a coupled ocean-atmosphere-wave-sediment transport modeling system. *Ocean Modelling*, *35*, 230–244.
Warner, J. C., Sherwood, C. R., Arango, H. G., & Signell, R. P. (2005). Performance of four turbulence closure models implemented using a generic length scale method. *Ocean Modelling*, *8*, 81–113.
Warner, J. C., Sherwood, C. R., Signell, R. P., Harris, C. K., & Arango, H. G. (2008). Development of a three-dimensional, regional, coupled wave, current, and sediment-transport model. *Computers & Geosciences*, *34*, 1284–1306.
Wilcox, D. C. (1988). Reassessment of the scale determining equation for advance turbulence models. *AIAA Journal*, *26*, 1299–1310.
Wilmott, C. J. (1981). On the validation of models. *Physical Geography*, *2*, 184–194.
Winterwerp, J. C. (1998). A simple model for turbulence induced flocculation of cohesive sediment. *Journal of Hydraulics Research*, *36*(3), 309–326.
Winterwerp, J. C., & van Kesteren, W. G. M. (2004). *Introduction to the physics of cohesive sediment in the marine environment*. Amsterdam, the Netherlands: Elsevier.
Zhang, Y. J., Ye, F., Stanev, E. V., & Grashorn, S. (2016). Seamless cross-scale modeling with schism. *Ocean Modelling*, *102*, 64–81.
Zhou, Z., van der Wegan, M., Jagers, B., & Coco, G. (2016). Modelling the role of self-weight consolidation on the morphodynamics of accretional mudflats. *Environmental Modelling & Software*, *76*, 167–181.